

# Shape optimization for maximizing ionic concentration constrained by steady-state Poisson-Nernst-Planck system\*

Jiajie Li <sup>†</sup>Shenggao Zhou <sup>‡</sup>Shengfeng Zhu <sup>§</sup>

June 17, 2024

## Abstract

We build a new mathematical model of shape optimization for maximizing ionic concentration governed by the multi-physical coupling steady-state Poisson-Nernst-Planck system. Shape sensitivity analysis is performed to obtain the Eulerian derivative of the cost functional. The Gummel fixed-point method with inverse harmonic averaging technique on exponential coefficient is used to solve efficiently the steady-state Poisson-Nernst-Planck system. Various numerical results using a shape gradient algorithm in 2d and 3d are presented.

**Keywords:** Shape optimization, Poisson-Nernst-Planck equation, shape sensitivity analysis, gradient flow, finite element

## 1 Introduction

With the developments in computer simulations, optimal shape design has attained significant achievements in computational fluid dynamics [24], structural mechanics [1, 3, 4], acoustics [25], photonic crystals [8], etc. Shape optimization has various applications in electrochemistry (cf. [11, 13, 23, 26, 31, 32]). For example, the design of vanadium redox flow batteries [31] was investigated for rechargeable batteries in the storage system of renewable energy resources conforming to low carbon emissions. A topology optimization framework is established for designing porous electrodes with a hierarchy of length scales for low-conductivity materials [28]. The level set method [20] is used for the design of anodes placed in an electroplating bath to achieve uniform deposition thickness. The optimized meso-scale structure for the electrolyte-anode interfaces of solid oxide fuel cells showed distinguished features [26]. The topological design of surface electrode distribution over piezoelectric sensors/actuators attached to a thin-walled shell structure was investigated [34] for reducing the sound radiation in an unbounded acoustic domain.

However, the governing system for modelling shape design in electrochemistry has been simplified in literature. In, e.g., [20, 26, 28], the change of concentration is neglected and the governing system involves only the Poisson equation of the chemical potential. PNP system [13] is typically used for describing the transport of charged particles in an electrical field. In this paper, we consider mathematical modelling and numerical methods on shape optimization of maximizing ionic concentration with a coupled multi-physical steady-state Poisson-Nernst-Planck system in electrochemistry.

For the sensitivity analysis of shape optimization, the *Eulerian derivative* of a *shape functional* can be expressed via the velocity method [30]. The *Eulerian derivative* is typically expressed in a boundary or domain formulation. The former one characterized by the Hadamard-Zolésio structure theorem [10] is popular due to its concise formula. Variational numerical methods based on boundary *Eulerian derivative* can perform shape changes in shape design [35]. The deduction of *Eulerian derivative* in boundary formulation involving extra introduction of the shape derivative thus requires more regularity on the computational domain. By the function space parametrization [10], the differentiability of the saddle point of a functional with respect to a real parameter give explicit expressions of the Eulerian derivative in domain formulation. For the Poisson-Nernst-Planck (PNP) system, the sensitivity analysis [12] is performed by a rigorous approach based on the sensitivity equation for the electrodiffusion model.

\*This work was supported in part by the National Key Basic Research Program under grant 2022YFA1004402, the Science and Technology Commission of Shanghai Municipality (No. 22ZR1421900 and 22DZ2229014), and the National Natural Science Foundation of China under grant (No. 12071149).

<sup>†</sup>School of Mathematical Sciences, Shanghai Jiao Tong University, Shanghai 200240, China. E-mail: lijiajie20120233@163.com

<sup>‡</sup>School of Mathematical Sciences, Shanghai Jiao Tong University, Shanghai 200240, China. E-mail: sgzhou@sjtu.edu.cn

<sup>§</sup>Key Laboratory of MEA (Ministry of Education) & Shanghai Key Laboratory of Pure Mathematics and Mathematical Practice & School of Mathematical Sciences, East China Normal University, Shanghai 200241, China. E-mail: sfzhu@math.ecnu.edu.cn

One of the most popular numerical schemes to solve steady-state PNP system is the Gummel fixed-point method [15, 22] which preserves excellent convergence properties even with rough initial guess. After introducing the Slotboom transformation, the scheme of the Gummel fixed-point method involves solving the semi-linear Poisson equation of potential and the decoupled continuity equation of concentration alternatively. The inverse harmonic averaging on exponential coefficients for the decoupled continuity equation in finite element discretization are proposed both in 2d [6] and 3d [33] to overcome numerical instability caused by strong advection. The quality of the mesh is essential to obtain the accurate concentration and potential functions [27, 6]. During shape evolutions, a smooth decent direction by a Cauchy-Riemann type gradient flow [19] and  $H^1$  gradient flow with uniform remeshing are used to keep shape regular and quasi-uniform meshes.

The rest of the paper is organized as follows. In Section 2, we briefly recall the PNP system in the dimensionless form. Both the Dirichlet and no-flux boundary conditions are imposed for the complicated chemical system. Then we build the shape optimization model to maximize the total concentration for all kinds of ionic species weighted by their valences under the volume constraint. In Section 3, we utilize the framework of velocity method for the PNP constrained optimal control problem to perform shape sensitivity analysis by introducing the corresponding adjoint equation. Both shape derivatives in domain and boundary expressions are derived in which the latter holds in the domain with more strict regularity. In Section 4, we introduce the augmented Lagrangian method to maintain the volume constraint during shape evolution. Then shape gradient algorithms are proposed by solving  $H^1$  or CT-H(sym) gradient flows to keep the domain moving in the decent direction while preserving the quality of the mesh. In Section 5, we consider the piece-wise linear finite element to solve the state, the adjoint state and gradient flow equation involved in the procedure of optimization algorithm. The Gummel iteration with exponential fitting technique is considered to solve the decoupled Poisson-Nernst-Planck system efficiently and accurately. In Section 6, various numerical experiments both in 2d and 3d spaces are presented to show the effectiveness of the algorithm proposed.

## 2 Model problem

We first formulate the steady-state PNP system and then build a mathematical shape optimization model with physically coupling PNP constraint and geometric volume constraint.

### 2.1 Governing system

Let  $\Omega \subset \mathbb{R}^d$  ( $d = 2, 3$ ) be an open bounded domain with Lipschitz continuous boundary  $\partial\Omega$ . Let  $c_i : \Omega \rightarrow \mathbb{R}$  ( $i = 1, \dots, N$ ) be the ionic concentration of the  $i$ -th species with its valence  $z_i$ , where  $N \in \mathbb{N}^+$  is the number of ionic species. Let  $\epsilon > 0$  be a coefficient arising from nondimensionalization and  $\phi$  be the electrostatic potential which describes the Coulomb interaction in a mean-field approximation. The domain  $\Omega$  is partitioned into two subdomains  $\bar{\Omega} = \bar{\Omega}_1 \cup \bar{\Omega}_2$  with the disjoint boundaries satisfying  $\partial\Omega = \bar{\Gamma}_{\text{in}} \cup \bar{\Gamma}_1 \cup \bar{\Gamma}_2$  (see Fig. 1). For the concentration function, no-flux condition is imposed on  $\Gamma_1$  and  $\Gamma_2$ , while the Dirichlet condition  $c_i^\infty : \Gamma_{\text{in}} \rightarrow \mathbb{R}$  is imposed on  $\Gamma_{\text{in}}$  simulating the ionic pool outside the computational domain to maintain the concentration invariant. For the electrostatic potential, consider both Dirichlet condition  $g : \Gamma_2 \rightarrow \mathbb{R}$  and homogeneous Neumann condition on the rest of boundary. The governing system of PNP system [13, 14] is given by: find each concentration  $c_i$  and potential  $\phi$  such that

$$\begin{cases} -\nabla \cdot (\nabla c_i + z_i c_i \nabla \phi) = 0, & \text{in } \Omega, \\ -\nabla \cdot \epsilon \nabla \phi = \sum_{i=1}^N z_i c_i, & \text{in } \Omega, \\ c_i = c_i^\infty, & \text{on } \Gamma_{\text{in}}, \\ \frac{\partial c_i}{\partial \mathbf{n}} + z_i c_i \frac{\partial \phi}{\partial \mathbf{n}} = 0, & \text{on } \Gamma_1 \cup \Gamma_2, \\ \frac{\partial \phi}{\partial \mathbf{n}} = 0, & \text{on } \Gamma_{\text{in}} \cup \Gamma_1, \\ \phi = g, & \text{on } \Gamma_2, \end{cases} \quad (1)$$

where  $\mathbf{n}$  is an outward unit normal on the boundary. In (1), the Nernst-Planck system describe the transport of the ions meanwhile the Poisson equation determines the electrostatic potential with the charge density arising from diffusing ions.

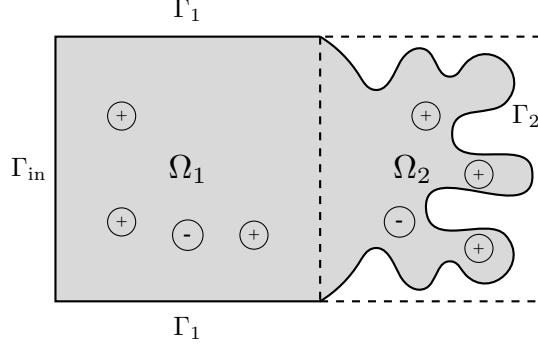


Figure 1: Schematic diagram of the design domain and boundary labels.

## 2.2 Shape optimization

A *shape functional* depending on a domain  $\Omega$  is denoted by a real-valued functional  $J(\Omega)$  with  $J(\cdot) : \Omega \mapsto \mathbb{R}$ . Governed by the coupling PNP system, consider the following shape functional describing the sum of ion concentrations weighted by the corresponding valences

$$J_0(\Omega) = \int_{\Omega} \mathbf{z}^T \mathbf{c} \, dx, \quad (2)$$

where  $\mathbf{c} = [c_1, c_2, \dots, c_N]^T$  and  $\mathbf{z} = [z_1, z_2, \dots, z_N]^T$ . Let the boundaries  $\Gamma_{\text{in}}$  and  $\Gamma_1$  be fixed while  $\Gamma_2$  is to be optimized (see Fig. 1). Denote the volumetric shape functional  $\mathcal{P}_1(\Omega)$  as the geometric Lebesgue measure of  $\Omega$ . One of the interesting topics in electrochemistry is to design the profile of the domain such that it can hold the ion as much as possible [2]. As generally a shape optimization model is not well-posed without a geometry (e.g., volume or perimeter) constraint, a volume constrained shape optimization model can be built as the following maximization problem

$$\max_{\Omega \in \mathcal{U}_{ad}} J_0(\Omega), \quad (3)$$

where  $\mathbf{c}$  is the solution of PNP (1) and the admissible set defines

$$\mathcal{U}_{ad} = \{\Omega \subset \mathbb{R}^d \mid \mathcal{P}_1(\Omega) = \mathcal{C}_1, \Omega \text{ is Lipschitz continuous}\}$$

with a prescribed  $\mathcal{C}_1 > 0$ . The shape optimization problem (3) can be converted into a standard minimization problem

$$\min_{\Omega \in \mathcal{U}_{ad}} J(\Omega), \quad (4)$$

where  $J(\Omega) = -J_0(\Omega)$ . Let  $\tilde{j}(\mathbf{c}) := \sum_{i=1}^N j(c_i)$  with each  $j(c_i) = -z_i c_i$ . Thus,  $\tilde{j}(\mathbf{c}) = \mathbf{z} \cdot \mathbf{c}$  and  $J(\Omega) = \int_{\Omega} \tilde{j}(\mathbf{c}) \, dx$ .

## 3 Shape sensitivity analysis

In this section, we perform *shape sensitivity analysis* based on the velocity method [30] to deduce the shape derivatives both in domain and boundary expressions. First of all, let us introduce notations for Sobolev spaces used. Denote the scalar Sobolev space for the potential function  $H_{\Gamma_2,d}^1(\Omega) := \{w \in H^1(\Omega) : w = g \text{ on } \Gamma_2\}$ , the vectorial Sobolev space  $\mathbf{H}^1(\Omega) := H^1(\Omega)^N$  and the scalar space  $H_{\Gamma_{\text{in}},i}^1(\Omega) := \{w \in H^1(\Omega) : w = c_i^\infty, \text{ on } \Gamma_{\text{in}}\}$  ( $i = 1, \dots, N$ ) for each concentration function. Denote  $\mathbf{H}_{\Gamma_{\text{in}},0}^1(\Omega) := \{\mathbf{w} \in \mathbf{H}^1(\Omega) : \mathbf{w} = \mathbf{0} \text{ on } \Gamma_{\text{in}}\}$  and  $H_{\Gamma_2,0}^1(\Omega) := \{w \in H^1(\Omega) : w = 0 \text{ on } \Gamma_2\}$  for the adjoint variables considered later. In the following, we briefly introduce the notation and framework of the velocity method.

### 3.1 Velocity method

The velocity method can be utilized for shape sensitivity analysis (see [10, 30]). Let  $\boldsymbol{\theta} \in C([0, \tau]; \mathcal{D}^1(\mathbb{R}^d, \mathbb{R}^d))$  be the velocity field characterizing shape deformation over the whole domain, where  $\mathcal{D}^1(\mathbb{R}^d, \mathbb{R}^d)$  denotes the space of all continuous differentiable functions with compact support contained in  $\mathbb{R}^d$  and  $\tau > 0$  is a sufficiently small number. For each  $0 < t < \tau$ , the velocity field is defined by  $\boldsymbol{\theta}(t)(\mathbf{x}) := \boldsymbol{\theta}(t, \mathbf{x}) \in \mathcal{D}^1(\mathbb{R}^d, \mathbb{R}^d)$ . Given  $\mathbf{X} \in \mathbb{R}^d$ , it generates a family of transformations

$$T_t(\boldsymbol{\theta})(\mathbf{X}) = \mathbf{x}(t, \mathbf{X}),$$

through the following dynamic system

$$\begin{cases} \frac{d\mathbf{x}}{dt}(t, \mathbf{X}) = \boldsymbol{\theta}(t, \mathbf{x}(t)), & t \in (0, \tau), \\ \mathbf{x}(0, \mathbf{X}) = \mathbf{X}, & t = 0. \end{cases}$$

The transformed domain  $T_t(\boldsymbol{\theta})(\Omega)$  is denoted by  $\Omega_t$ . Next, some elementary definitions on shape calculus are listed as follows [10, 30].

**Definition 3.1.** Let  $J(\Omega)$  be a real-valued shape functional  $J(\cdot) : \Omega \mapsto \mathbb{R}$ . The Eulerian derivative of  $J(\Omega)$  at  $\Omega$  in the direction  $\boldsymbol{\theta} \in C([0, \tau]; \mathcal{D}^1(\mathbb{R}^d, \mathbb{R}^d))$  is defined by the limit

$$dJ(\Omega; \boldsymbol{\theta}) := \lim_{t \rightarrow 0^+} \frac{J(\Omega_t) - J(\Omega)}{t}.$$

**Definition 3.2.** [30, 16] The material derivative of a scalar state variable  $w \in H^1(\Omega)$  in a direction  $\boldsymbol{\theta} \in C([0, \tau]; \mathcal{D}^1(\mathbb{R}^d, \mathbb{R}^d))$  is defined by

$$\dot{w}(\Omega; \boldsymbol{\theta}) := \lim_{t \rightarrow 0^+} \frac{w(\Omega_t) \circ T_t(\Omega) - w(\Omega)}{t},$$

if the limit exists. Then for a vectorial state variable  $\mathbf{w} := [w_1, w_2, \dots, w_N]^T$ , its material derivative is defined by  $\dot{\mathbf{w}} := [\dot{w}_1, \dot{w}_2, \dots, \dot{w}_N]^T$ .

**Definition 3.3.** The shape derivative of  $w$  in the direction  $\boldsymbol{\theta}$  is the element  $w'(\Omega; \boldsymbol{\theta}) \in H^1(\Omega)$  defined by

$$w'(\Omega; \boldsymbol{\theta}) := \dot{w}(\Omega; \boldsymbol{\theta}) - \nabla w \cdot \boldsymbol{\theta}(0).$$

Then for a vectorial state variable  $\mathbf{w} := [w_1, w_2, \dots, w_N]^T \in \mathbf{H}^1(\Omega)$ , its shape derivative is defined by

$$\mathbf{w}' := [w'_1, w'_2, \dots, w'_N]^T.$$

Suppose that the boundary is sufficiently smooth enough. Then the following tangential gradient and divergence operators are available, respectively.

**Definition 3.4.** Let the design domain is of  $C^2$  class with  $\mathbf{n}$  being the unit outward normal vector defined on its boundary  $\partial\Omega$ . Let  $U$  be an open bounded set such that  $\partial\Omega \subset U$ .

- The tangential divergence of vectorial variable  $\mathbf{w} \in C^1(U; \mathbb{R}^d)$  along the boundary is defined by

$$\text{div}_\Gamma \mathbf{w} := \text{div} \mathbf{w} - \mathbf{n}^T \mathbf{D} \mathbf{w} \mathbf{n},$$

where  $\text{div}(\cdot)$  and  $\mathbf{D}(\cdot)$  are the standard divergence and vectorial gradient operators defined on  $\mathbf{H}^1(U)$ .

- The tangential gradient  $\nabla_\Gamma$  of scalar variable  $w \in C^1(U; \mathbb{R})$  on the boundary is defined by

$$\nabla_\Gamma w := \nabla w - \frac{\partial w}{\partial \mathbf{n}} \mathbf{n}.$$

**Proposition 3.5.** [16] Let the deformation field  $\boldsymbol{\theta} = [\theta_1, \theta_2, \dots, \theta_d]^T \in W^{1,\infty}(\Omega)^d$ . Then the following equations hold

$$\begin{aligned} (1) \quad DT_t|_{t=0} &= \text{Id}, & (2) \quad \frac{d}{dt} T_t \Big|_{t=0} &= \boldsymbol{\theta}, \\ (3) \quad \frac{d}{dt} DT_t \Big|_{t=0} &= \mathbf{D} \boldsymbol{\theta} = \left( \frac{\partial \theta_i}{\partial x_j} \right)_{i,j=1}^d, & (4) \quad \frac{d}{dt} DT_t^T \Big|_{t=0} &= \mathbf{D} \boldsymbol{\theta}^T, \\ (5) \quad \frac{d}{dt} (DT_t^{-1}) \Big|_{t=0} &= -\mathbf{D} \boldsymbol{\theta}, & (6) \quad \frac{d}{dt} J_t \Big|_{t=0} &= \text{div} \boldsymbol{\theta}. \end{aligned}$$

For shape optimization, apart from some geometric constraints, it generally has physical state constraints. Treating the state system as an equality constraint and using Lagrange multiplier method commonly yields dual variables which are solution of the adjoint system.



**Lemma 3.6.** *The adjoint system to the optimization problem (4) constrained by (1) is to find  $(\mathbf{s}, \psi) \in \mathbf{H}^2(\Omega) \times H^2(\Omega)$  with the vectorial valued function  $\mathbf{s} = [s_1, s_2, \dots, s_N]^T$  such that the following coupled system with the mixed boundary conditions*

$$\begin{cases} -\Delta s_i + z_i \nabla \phi \cdot \nabla s_i - z_i \psi = -j'(c_i), & \text{in } \Omega, \\ -\epsilon \Delta \psi = \sum_{i=1}^N \nabla \cdot (z_i c_i \nabla s_i), & \text{in } \Omega, \\ s_i = 0, & \text{on } \Gamma_{\text{in}}, \\ \frac{\partial s_i}{\partial \mathbf{n}} = 0, & \text{on } \Gamma_1 \cup \Gamma_2, \\ \psi = 0, & \text{on } \Gamma_2, \\ \frac{\partial \psi}{\partial \mathbf{n}} = 0, & \text{on } \Gamma_{\text{in}} \cup \Gamma_1. \end{cases} \quad (5)$$

*Proof.* By considering the weak formulation of the PNP (1), define the following functional with the boundary constraints

$$\begin{aligned} \mathcal{G}(\Omega, \mathbf{c}, \phi, \mathbf{s}, \psi, \Lambda) = & \sum_{i=1}^N \int_{\Omega} (\nabla c_i + z_i c_i \nabla \phi) \cdot \nabla s_i \, dx + \int_{\Omega} \epsilon \nabla \phi \cdot \nabla \psi - \sum_{i=1}^N z_i c_i \psi \, dx \\ & + \int_{\Gamma_2} \lambda_0 (\phi - g) \, ds + \sum_{i=1}^N \int_{\Gamma_{\text{in}}} \lambda_i (c_i - c_i^{\infty}) \, ds, \end{aligned} \quad (6)$$

where  $\Lambda = [\lambda_0, \lambda_1, \dots, \lambda_N]^T \in L^2(\partial\Omega)^{N+1}$  is a multiplier vector. Let the test functions are such that  $(\mathbf{s}, \psi) \in \mathbf{H}_{\Gamma_{\text{in}},0}^1(\Omega) \times H_{\Gamma_2,0}^1(\Omega)$ . Then the Lagrange functional  $\mathcal{L}(\Omega, \mathbf{c}, \phi, \mathbf{s}, \psi, \Lambda)$  is introduced by the summation of (6) and the objective (4)

$$\mathcal{L}(\Omega, \mathbf{c}, \phi, \mathbf{s}, \psi, \Lambda) := J(\Omega) + \mathcal{G}(\Omega, \mathbf{c}, \phi, \mathbf{s}, \psi, \Lambda). \quad (7)$$

The shape functional (4) with constraints (1) can be transformed equivalently into the following min-max formulation (see [10])

$$J(\Omega) = \min_{(\mathbf{c}, \phi)} \max_{(\mathbf{s}, \psi, \Lambda)} \mathcal{L}(\Omega, \mathbf{c}, \phi, \mathbf{s}, \psi, \Lambda). \quad (8)$$

By the Karush-Kuhn-Tucker condition, the saddle point of  $\mathcal{L}$  is characterized by

$$\frac{\partial \mathcal{L}}{\partial s_i}(\delta s_i) = \frac{\partial \mathcal{L}}{\partial \psi}(\delta \psi) = \frac{\partial \mathcal{L}}{\partial \Lambda}(\delta \Lambda) = 0 \quad \forall \delta s_i, \delta \psi \in H^1(\Omega), \delta \Lambda \in L^2(\partial\Omega)^{N+1}, \quad (9)$$

as well as

$$\frac{\partial \mathcal{L}}{\partial c_i}(\delta c_i) = \frac{\partial \mathcal{L}}{\partial \phi}(\delta \phi) = 0 \quad \forall \delta c_i, \delta \phi \in H^1(\Omega). \quad (10)$$

Eq. (9) yields the weak formulation of PNP system (6). On the other hand, Eq. (10) implies the adjoint state system which we shall derive as follows. Firstly, the Fréchet derivative of the Lagrangian (7) with respect to each concentration variable gives the first-order optimality condition:

$$\begin{aligned} 0 = \frac{\partial \mathcal{L}}{\partial c_i}(\delta c_i) = & \int_{\Omega} j'(c_i) \delta c_i + (\nabla \delta c_i + z_i \delta c_i \nabla \phi) \cdot \nabla s_i \, dx - \int_{\Omega} z_i \delta c_i \psi \, dx + \int_{\Gamma_{\text{in}}} \lambda_i \delta c_i \, ds \\ = & \int_{\Omega} j'(c_i) \delta c_i - \Delta s_i \delta c_i + z_i \nabla \phi \cdot \nabla s_i \delta c_i - z_i \psi \delta c_i \, dx + \int_{\Gamma_{\text{in}}} \frac{\partial s_i}{\partial \mathbf{n}} \delta c_i \, ds + \int_{\Gamma_{\text{in}}} \lambda_i \delta c_i \, ds \\ & + \int_{\Gamma_1 \cup \Gamma_2} \frac{\partial s_i}{\partial \mathbf{n}} \delta c_i \, ds, \end{aligned} \quad (11)$$

which by the density property implies that

$$\begin{cases} -\Delta s_i + z_i \nabla \phi \cdot \nabla s_i - z_i \psi = -j'(c_i), & \text{in } \Omega, \\ \frac{\partial s_i}{\partial \mathbf{n}} = 0, & \text{on } \Gamma_1 \cup \Gamma_2, \\ s_i = 0, & \text{on } \Gamma_{\text{in}}, \\ \lambda_i = -\frac{\partial s_i}{\partial \mathbf{n}}. \end{cases} \quad (12)$$

Secondly, the Fréchet derivative of the Lagrangian (7) with respect to potential gives the optimality condition

$$\begin{aligned} 0 = \frac{\partial \mathcal{G}}{\partial \phi}(\delta \phi) &= \sum_{i=1}^N \int_{\Omega} z_i c_i \nabla \delta \phi \cdot \nabla s_i \, dx + \int_{\Omega} \epsilon \nabla \delta \phi \cdot \nabla \psi + \int_{\partial \Omega} \lambda_0 \delta \phi \, ds, \\ &= \int_{\Omega} - \sum_{i=1}^N \nabla \cdot (z_i c_i \nabla s_i) \delta \phi - \epsilon \Delta \psi \delta \phi \, dx + \int_{\partial \Omega} \left( \sum_{i=1}^N z_i c_i \frac{\partial s_i}{\partial \mathbf{n}} + \epsilon \frac{\partial \psi}{\partial \mathbf{n}} + \lambda_0 \right) \delta \phi \, ds, \end{aligned} \quad (13)$$

which by the density property yields that

$$\begin{cases} -\epsilon \Delta \psi = \sum_{i=1}^N \nabla \cdot (z_i c_i \nabla s_i), & \text{in } \Omega, \\ \psi = 0, & \text{on } \Gamma_2, \\ \frac{\partial \psi}{\partial \mathbf{n}} = 0, & \text{on } \Gamma_{\text{in}} \cup \Gamma_1, \\ \lambda_0 = - \sum_{i=1}^N z_i c_i \frac{\partial s_i}{\partial \mathbf{n}} - \epsilon \frac{\partial \psi}{\partial \mathbf{n}}. \end{cases} \quad (14)$$

To sum up the above arguments, the strong form of the adjoint system (5) holds.  $\square$

### 3.2 Shape sensitivity

The shape sensitivity analysis is based on the framework of Lagrangian method [10] by introducing a Lagrangian functional to convert the original constrained optimization problem into a saddle point problem. We introduce the following *function space parametrization* method [10, Section 5.3]. For the state and adjoint state function defined on the perturbed domain  $\Omega_t$ , we have the following parametrization

$$H^1(\Omega_t) = \{\phi \circ T_t^{-1} : \phi \in H^1(\Omega)\},$$

where  $t$  small enough such that  $T_t$  and  $T_t^{-1}$  are diffeomorphisms. Lagrangian methods in shape optimization allow to calculate the Eulerian derivative of shape functional depending on the solution of governing system without the need to calculate the material derivative of the state variables. For any vector function  $\mathbf{w} = [w_1, w_2, \dots, w_N]^T$  and  $\mathbf{z} = [z_1, z_2, \dots, z_N]^T$ , the Frobenius inner product for (tangential) gradient is defined by  $D\mathbf{w} : D\mathbf{z} := \sum_{i=1}^N \nabla w_i \cdot \nabla z_i$  and  $D_{\Gamma} \mathbf{w} : D_{\Gamma} \mathbf{z} := \sum_{i=1}^N \nabla_{\Gamma} w_i \cdot \nabla_{\Gamma} z_i$ , respectively.

**Theorem 3.7.** *Let the  $\Omega$  be bounded domain with Lipschitz continuous boundary. Suppose that  $(\mathbf{c}, \phi)$  is the solution of (1) and  $(\mathbf{s}, \psi)$  is the solution of adjoint problem (5). Then the Eulerian derivative of functional (4) in domain expression is given by*

$$dJ_{\mathcal{V}}(\Omega, \boldsymbol{\theta}) = \int_{\Omega} (-\mathbf{z}^T \mathbf{c} \psi - \mathbf{z}^T \mathbf{c}) \operatorname{div} \boldsymbol{\theta} + M(\boldsymbol{\theta}) D\mathbf{c} : D\mathbf{s} + M(\boldsymbol{\theta}) D\Phi : (D\mathbf{s} \mathbf{Z} \mathbf{C}) + \epsilon M(\boldsymbol{\theta}) \nabla \phi \cdot \nabla \psi \, dx, \quad (15)$$

where the matrix function denotes  $M(\boldsymbol{\theta}) := \operatorname{div} \boldsymbol{\theta} \operatorname{Id} - D\boldsymbol{\theta}^T - D\boldsymbol{\theta}$  and

$$\mathbf{Z} := \operatorname{diag}[z_1, z_2, \dots, z_N], \quad \mathbf{C} := \operatorname{diag}[c_1, c_2, \dots, c_N], \quad \Phi := \phi I_N,$$

with  $\operatorname{diag}$  denoting the diagonal matrix of some vector and  $I_N$  denoting the vector of size  $N$  with each element being 1 and  $\operatorname{Id}$  is the identity matrix.

*Proof.* Introduce a Lagrangian with Lagrange multipliers as

$$\mathcal{L}(\Omega, \mathbf{c}, \phi, \mathbf{s}, \psi) = \sum_{i=1}^N \int_{\Omega} j(c_i) \, dx + \sum_{i=1}^N \int_{\Omega} (\nabla c_i + z_i c_i \nabla \phi) \cdot \nabla s_i \, dx + \int_{\Omega} \epsilon \nabla \phi \cdot \nabla \psi - \sum_{i=1}^N z_i c_i \psi \, dx, \quad (16)$$

where  $\mathbf{s}$  and  $\psi$  are adjoint variables satisfying (5). Then the functional  $\mathcal{L}$  on perturbed domain reads:

$$\begin{aligned} \mathcal{L}(\Omega_t, \mathbf{c}_t, \phi_t, \mathbf{s}_t, \psi_t) &= \sum_{i=1}^N \int_{\Omega_t} j(c_{i,t}) \, dx + \sum_{i=1}^N \int_{\Omega_t} (\nabla c_{i,t} + z_i c_{i,t} \nabla \phi_t) \cdot \nabla s_{i,t} \, dx \\ &\quad + \int_{\Omega_t} \epsilon \nabla \phi_t \cdot \nabla \psi_t - \sum_{i=1}^N z_i c_{i,t} \psi_t \, dx, \end{aligned} \quad (17)$$

with each  $c_{i,t} \in H_{\Gamma_{\text{in},i}}^1(\Omega_t)$ ,  $s_{i,t} \in H^1(\Omega_t)$ ,  $\phi_t \in H_{\Gamma_{2,d}}^1(\Omega_t)$  and  $\psi_t \in H^1(\Omega_t)$ . The objective  $J(\Omega_t)$  can be expressed as a min-max of the functional  $\mathcal{L}$  with saddle point characterized by

$$J(\Omega_t) = \min_{(\mathbf{c}_t, \phi_t)} \max_{(\mathbf{s}_t, \psi_t)} \mathcal{L}(\Omega_t, \mathbf{c}_t, \phi_t, \mathbf{s}_t, \psi_t).$$

A new Lagrangian with parametrization is introduced for all  $\mathbf{c}, \mathbf{s} \in \mathbf{H}^1(\Omega)$  and  $\phi, \psi \in H^1(\Omega)$

$$\tilde{\mathcal{L}}(t, \mathbf{c}, \phi, \mathbf{s}, \psi) = \mathcal{L}(\Omega_t, \mathbf{c} \circ T_t^{-1}, \phi \circ T_t^{-1}, \mathbf{s} \circ T_t^{-1}, \psi \circ T_t^{-1}). \quad (18)$$

By definition,  $\tilde{\mathcal{L}}$  is given by the expression

$$\begin{aligned} \tilde{\mathcal{L}}(t, \mathbf{c}, \phi, \mathbf{s}, \psi) &= \sum_{i=1}^N \int_{\Omega_t} -z_i(c_i \circ T_t^{-1}) \, dx \\ &+ \sum_{i=1}^N \int_{\Omega_t} [\nabla(c_i \circ T_t^{-1}) + z_i(c_i \circ T_t^{-1}) \nabla(\phi \circ T_t^{-1})] \cdot \nabla(s_i \circ T_t^{-1}) \, dx \\ &+ \int_{\Omega_t} \epsilon \nabla(\phi \circ T_t^{-1}) \cdot \nabla(\psi \circ T_t^{-1}) - \sum_{i=1}^N z_i(c_i \circ T_t^{-1})(\psi \circ T_t^{-1}) \, dx, \end{aligned} \quad (19)$$

where  $c_i \circ T_t^{-1} = c_{i,t}$ ,  $s_i \circ T_t^{-1} = s_{i,t}$ ,  $\phi \circ T_t^{-1} = \phi_t$  and  $\psi \circ T_t^{-1} = \psi_t$ . We can rewrite expressions (19) on the fixed domain  $\Omega$  by using the transformation  $T_t$ . Hence (19) becomes

$$\begin{aligned} \tilde{\mathcal{L}}(t, \mathbf{c}, \phi, \mathbf{s}, \psi) &= \sum_{i=1}^N \int_{\Omega} -z_i c_i J_t \, dx + \sum_{i=1}^N \int_{\Omega} \mathcal{A}(t) \nabla c_i \cdot \nabla s_i + z_i \mathcal{A}(t) c_i \nabla \phi \cdot \nabla s_i \, dx \\ &+ \int_{\Omega} \epsilon \mathcal{A}(t) \nabla \phi \cdot \nabla \psi - \sum_{i=1}^N z_i c_i \psi J_t \, dx, \end{aligned} \quad (20)$$

where the determinant  $J_t = \det DT_t$  and  $\mathcal{A}(t) = J_t [DT_t]^{-1} [DT_t]^{-T}$ . For all state and adjoint variables,  $\tilde{\mathcal{L}}(t, \cdot)$  is differentiable with respect to  $t$ . Thus, it yields that

$$\begin{aligned} \partial_t \tilde{\mathcal{L}}(t, \mathbf{c}, \phi, \mathbf{s}, \psi) &= \sum_{i=1}^N \int_{\Omega} -z_i c_i J'_t \, dx + \sum_{i=1}^N \int_{\Omega} \mathcal{A}'(t) \nabla c_i \cdot \nabla s_i + z_i \mathcal{A}'(t) c_i \nabla \phi \cdot \nabla s_i \, dx \\ &+ \int_{\Omega} \epsilon \mathcal{A}'(t) \nabla \phi \cdot \nabla \psi - \sum_{i=1}^N z_i c_i \psi J'_t \, dx. \end{aligned} \quad (21)$$

Using the properties that

$$\begin{aligned} \mathcal{Q}'(t) &= -\mathcal{Q}(t) D\boldsymbol{\theta}(t) \circ T_t, \\ \mathcal{A}'(t) \boldsymbol{\tau} : \boldsymbol{\sigma} &= [\boldsymbol{\tau} \mathcal{Q}'(t)] : [\boldsymbol{\sigma} \mathcal{Q}(t)] + [\boldsymbol{\tau} \mathcal{Q}(t)] : [\boldsymbol{\sigma} \mathcal{Q}'(t)], \\ J'_t &= \text{div} \boldsymbol{\theta}(t), \end{aligned} \quad (22)$$

where  $\mathcal{Q}(t) := (DT_t)^{-1}$ , we obtain

$$\mathcal{A}'(0) \boldsymbol{\tau} : \boldsymbol{\sigma} = -[(D\boldsymbol{\tau} D\boldsymbol{\theta}(0) : D\boldsymbol{\sigma}) + (D\boldsymbol{\tau} : D\boldsymbol{\sigma} D\boldsymbol{\theta}(0))]. \quad (23)$$

By the Correa-Seeger Theorem [10], the Eulerian derivative in domain expression can be obtained as

$$\begin{aligned} dJ_{\mathcal{V}}(\Omega, \boldsymbol{\theta}) &= \partial_t \tilde{\mathcal{L}}(0, \mathbf{c}, \phi, \mathbf{s}, \psi) \\ &= \sum_{i=1}^N \int_{\Omega} -z_i c_i \text{div} \boldsymbol{\theta} + (\text{div} \boldsymbol{\theta} \text{Id} - D\boldsymbol{\theta}^T - D\boldsymbol{\theta}) \nabla c_i \cdot \nabla s_i + z_i c_i (\text{div} \boldsymbol{\theta} \text{Id} - D\boldsymbol{\theta}^T - D\boldsymbol{\theta}) \nabla \phi \cdot \nabla s_i \, dx \\ &+ \int_{\Omega} \epsilon (\text{div} \boldsymbol{\theta} \text{Id} - D\boldsymbol{\theta}^T - D\boldsymbol{\theta}) \nabla \phi \cdot \nabla \psi - \sum_{i=1}^N z_i c_i \psi \text{div} \boldsymbol{\theta} \, dx, \end{aligned} \quad (24)$$

where  $\boldsymbol{\theta} := \boldsymbol{\theta}(0)$  for simplicity. After matrix and vector rearrangements, the shape derivative in domain expression is given by the matrix formulation (15).  $\square$

Next, we are going to deduce the shape gradient in boundary formula. It requires that the boundary is of  $C^2$  class with strict regularity. The shape derivative of function  $c_i$  and  $\phi$  are characterized by the following Lemma.

**Lemma 3.8.** Suppose that the boundary  $\Omega$  is of  $C^2$  class. Let  $(c_i, \phi)$  be the solution of PNP system (1). Then the shape derivative  $(c'_i, \phi')$  satisfies that

$$\begin{cases} -\Delta c'_i - \nabla \cdot (z_i c'_i \nabla \phi + z_i c_i \nabla \phi') = 0, & \text{in } \Omega, \\ -\epsilon \Delta \phi' = \mathbf{z}^T \mathbf{c}', & \text{in } \Omega, \\ (\nabla c'_i + z_i c'_i \nabla \phi + z_i c_i \nabla \phi') \cdot \mathbf{n} = \operatorname{div}_\Gamma[\boldsymbol{\theta} \cdot \mathbf{n}(\nabla c_i + z_i c_i \nabla \phi)], & \text{on } \partial\Omega, \\ \phi' = -\frac{\partial(\phi - g)}{\partial \mathbf{n}} \boldsymbol{\theta}_n, & \text{on } \partial\Omega, \end{cases} \quad (25)$$

where the shape derivative of the vectorial function denotes  $\mathbf{c}' := [c'_1, c'_2, \dots, c'_N]$  and  $\boldsymbol{\theta}_n := \boldsymbol{\theta} \cdot \mathbf{n}$ .

*Proof.* The weak formulation of Nernst-Planck system in (1) with boundary conditions on the perturbed domain is to seek  $c_{i,t} \in H^1_{\Gamma_{in},i}(\Omega_t)$  and  $\phi_t \in H^1_{\Gamma_2,d}(\Omega_t)$  such that

$$\int_{\Omega_t} (\nabla c_{i,t} + z_i c_{i,t} \nabla \phi_t) \cdot \nabla v \, dx = 0, \quad \forall v \in H^1(\mathbb{R}^d). \quad (26)$$

Recalling the Hadamard's formula [17], for a sufficiently smooth function  $F : [0, \tau] \times \mathbb{R}^d \rightarrow \mathbb{R}$ , it holds that

$$\left. \frac{d}{dt} \int_{\Omega_t} F(t, \mathbf{x}) \, dx \right|_{t=0} = \int_{\partial\Omega} F(0, \mathbf{x}) \boldsymbol{\theta}(0) \cdot \mathbf{n} \, ds + \int_{\Omega} \frac{\partial F}{\partial t}(0, \mathbf{x}) \, dx. \quad (27)$$

Then the shape derivatives satisfies that

$$\int_{\Omega} (\nabla c'_i + z_i c'_i \nabla \phi + z_i c_i \nabla \phi') \cdot \nabla v \, dx + \int_{\partial\Omega} (\nabla c_i + z_i c_i \nabla \phi) \cdot \nabla v \boldsymbol{\theta}_n \, ds = 0 \quad \forall v \in H^1(\mathbb{R}^d). \quad (28)$$

Using the integration by parts yields that

$$\begin{aligned} & \int_{\Omega} -\Delta c'_i v - \nabla \cdot (z_i c'_i \nabla \phi + z_i c_i \nabla \phi') v \, dx + \int_{\partial\Omega} \frac{\partial c'_i}{\partial \mathbf{n}} v + (z_i c'_i \nabla \phi + z_i c_i \nabla \phi') \cdot \mathbf{n} v \, ds \\ & + \int_{\partial\Omega} (\nabla c_i + z_i c_i \nabla \phi) \cdot \nabla v \boldsymbol{\theta}_n \, ds = 0. \end{aligned} \quad (29)$$

Taking the test function  $v$  with a compact support in  $\Omega$  implies that

$$-\Delta c'_i - \nabla \cdot (z_i c'_i \nabla \phi + z_i c_i \nabla \phi') = 0 \quad \text{in } \Omega. \quad (30)$$

Taking test function with homogeneous Neumann condition  $\frac{\partial v}{\partial \mathbf{n}} = 0$ , we obtain

$$\int_{\partial\Omega} \frac{\partial c'_i}{\partial \mathbf{n}} v + (z_i c'_i \nabla \phi + z_i c_i \nabla \phi') \cdot \mathbf{n} v \, ds + \int_{\partial\Omega} (\nabla c_i + z_i c_i \nabla \phi) \cdot \nabla v \boldsymbol{\theta}_n \, ds = 0. \quad (31)$$

By density property and tangential Green's formula, we have the boundary condition for shape derivative

$$(\nabla c'_i + z_i c'_i \nabla \phi + z_i c_i \nabla \phi') \cdot \mathbf{n} = \operatorname{div}_\Gamma[\boldsymbol{\theta}_n(\nabla c_i + z_i c_i \nabla \phi)] \quad \text{on } \partial\Omega. \quad (32)$$

Similarly, the weak formulation of the Poisson equation in (1) for  $\phi_t$  on the perturbed domain reads:

$$\int_{\Omega_t} \epsilon \nabla \phi_t \cdot \nabla v \, dx = \int_{\Omega_t} \sum_{i=1}^N z_i c_{i,t} v \, dx \quad \forall v \in C_0^\infty(\Omega). \quad (33)$$

Hence, utilizing Hadamard's formula and compact support for test function yields that

$$\int_{\Omega} \epsilon \nabla \phi' \cdot \nabla v \, dx = \int_{\Omega} \sum_{i=1}^N z_i c'_i v \, dx. \quad (34)$$

By density property and integration by parts, we obtain the shape derivative for potential satisfying

$$-\epsilon \Delta \phi' = \sum_{i=1}^N z_i c'_i, \quad x \in \Omega, \quad (35)$$

The material derivative and tangential derivative hold that  $\dot{\phi} = \dot{g} = \nabla g \cdot \boldsymbol{\theta}$  and  $\nabla_\Gamma(\phi - g) = 0$ . Therefore for the boundary condition of the shape derivative, it can be deduced that

$$\phi' = \dot{\phi} - \nabla \phi \cdot \boldsymbol{\theta} = (\nabla g - \nabla \phi) \cdot \boldsymbol{\theta} = -\frac{\partial(\phi - g)}{\partial \mathbf{n}} \boldsymbol{\theta}_n \quad \text{on } \partial\Omega. \quad (36)$$

Above all, we deduce the system (25) for the shape derivative of states with respect to deformation field.  $\square$

We are prepared to deduce the Eulerian derivative of shape functional in boundary expression.

**Theorem 3.9.** *Let the boundary  $\Omega$  is of  $C^2$  class. Suppose that  $(\mathbf{c}, \phi)$  is the solution of PNP (1) and  $(\mathbf{s}, \psi)$  is the solution of adjoint problem (3.6). Then the shape derivative of functional (4) is given by*

$$dJ_S(\Omega, \boldsymbol{\theta}) = \int_{\Gamma_2} \left[ (\mathbf{D}_\Gamma \mathbf{c} + \mathbf{ZCD}_\Gamma \Phi) : \mathbf{D}_\Gamma \mathbf{s} + \tilde{j}(\mathbf{c}) - \frac{\partial(\phi - g)}{\partial \mathbf{n}} \frac{\partial \psi}{\partial \mathbf{n}} \right] \theta_n ds, \quad (37)$$

with the tangential gradient matrix defined by  $\mathbf{D}_\Gamma \mathbf{w} := [\nabla w_1, \nabla w_2, \dots, \nabla w_N]$  for all  $\mathbf{w} \in \mathbf{H}^1(\Omega)$ .

*Proof.* By Lemma 3.8, the weak variational forms of (25) with test functions  $(s_i, \psi)$  are

$$\int_{\Omega} (\nabla c'_i + z_i c'_i \nabla \phi + z_i c_i \nabla \phi') \cdot \nabla s_i dx = \int_{\partial \Omega} \operatorname{div}_\Gamma [\theta_n (\nabla c_i + z_i c_i \nabla \phi)] s_i ds, \quad (38)$$

and

$$\int_{\Omega} \epsilon \nabla \phi' \cdot \nabla \psi dx = \int_{\Omega} \sum_{i=1}^N z_i c'_i \psi dx. \quad (39)$$

Furthermore by Lemma 3.6, the weak formulations of adjoint system (5) with test functions  $(c'_i, \phi')$  are given by

$$\begin{cases} \int_{\Omega} \nabla s_i \cdot \nabla c'_i + z_i \nabla \phi \cdot \nabla s_i c'_i - z_i \psi c'_i + j'(c_i) c'_i dx = 0, \\ \int_{\Omega} -\epsilon \Delta \psi \phi' dx = \int_{\Omega} \sum_{i=1}^N \nabla \cdot (z_i c_i \nabla s_i) \phi' dx. \end{cases} \quad (40)$$

The property of the deformation field  $\boldsymbol{\theta}$  vanishing on  $\Gamma_{\text{in}} \cup \Gamma_1$  will be used in the following analysis. By the Hadamard's formula and the weak formulation (40), we have

$$\begin{aligned} dJ_S(\Omega, \boldsymbol{\theta}) &= \sum_{i=1}^N \int_{\Omega} j'(c_i) c'_i dx + \int_{\partial \Omega} \tilde{j}(\mathbf{c}) \theta_n ds \\ &= - \sum_{i=1}^N \int_{\Omega} \nabla s_i \cdot \nabla c'_i + z_i \nabla \phi \cdot \nabla s_i c'_i - z_i \psi c'_i dx + \int_{\partial \Omega} \tilde{j}(\mathbf{c}) \theta_n ds \\ &= - \sum_{i=1}^N \int_{\Omega} \nabla s_i \cdot \nabla c'_i + z_i \nabla \phi \cdot \nabla s_i c'_i dx + \int_{\Omega} \epsilon \nabla \phi' \cdot \nabla \psi dx + \int_{\Gamma_2} \tilde{j}(\mathbf{c}) \theta_n ds, \end{aligned} \quad (41)$$

where (39) is used for the last equality. From the integration by parts, it yields that

$$\begin{aligned} \int_{\Omega} \epsilon \nabla \phi' \cdot \nabla \psi dx &= - \int_{\Omega} \epsilon \Delta \psi \phi' dx + \int_{\partial \Omega} \epsilon \frac{\partial \psi}{\partial \mathbf{n}} \phi' ds \\ &= - \int_{\partial \Omega} \epsilon \frac{\partial \psi}{\partial \mathbf{n}} \frac{\partial(\phi - g)}{\partial \mathbf{n}} \theta_n ds + \int_{\Omega} \sum_{i=1}^N \nabla \cdot (z_i c_i \nabla s_i) \phi' dx \\ &= - \int_{\Gamma_2} \epsilon \frac{\partial \psi}{\partial \mathbf{n}} \frac{\partial(\phi - g)}{\partial \mathbf{n}} \theta_n ds - \int_{\Omega} \sum_{i=1}^N (z_i c_i \nabla s_i) \cdot \nabla \phi' dx, \end{aligned} \quad (42)$$

where the boundary condition in (25) is used for the second equality and the boundary term generated by the integration by parts for the last equality vanishes due to the homogeneous Neumann condition of  $s_i$ . From (28) by setting the test function  $v = s_i$ , we further obtain

$$\begin{aligned} dJ_S(\Omega, \boldsymbol{\theta}) &= - \sum_{i=1}^N \int_{\Omega} \nabla s_i \cdot \nabla c'_i + z_i \nabla \phi \cdot \nabla s_i c'_i + (z_i c_i \nabla s_i) \cdot \nabla \phi' dx + \int_{\Gamma_2} \tilde{j}(\mathbf{c}) \theta_n - \epsilon \frac{\partial \psi}{\partial \mathbf{n}} \frac{\partial(\phi - g)}{\partial \mathbf{n}} \theta_n ds \\ &= \int_{\Gamma_2} \left\{ \sum_{i=1}^N \left[ (\nabla_\Gamma c_i + z_i c_i \nabla_\Gamma \phi) \cdot \nabla_\Gamma s_i \right] + \tilde{j}(\mathbf{c}) - \epsilon \frac{\partial(\phi - g)}{\partial \mathbf{n}} \frac{\partial \psi}{\partial \mathbf{n}} \right\} \theta_n ds, \end{aligned} \quad (43)$$

where no flux condition is considered for the last equality. After some matrix and vector calculations, we obtain the shape gradient in boundary formula (37).  $\square$

## 4 Optimization algorithm

In this section, we propose a numerical shape gradient algorithm to solve the shape optimization problem.

## 4.1 Augmented Lagrangian method

The volume or perimeter constrained optimization model (4) can be transformed to an unconstrained optimization model by the augmented Lagrangian method [29]. The volume constraint is controlled by adding both variable coefficient linear and constant coefficient quadratic penalty terms. We introduce the augmented Lagrangian

$$\mathcal{L}(\Omega) = J(\Omega) + l(\mathcal{P}_1(\Omega) - \mathcal{C}_1) + \frac{1}{2}\beta(\mathcal{P}_1(\Omega) - \mathcal{C}_1)^2, \quad (44)$$

where  $l > 0$  denotes a Lagrange multiplier and  $\beta > 0$  is a penalty parameter. The Eulerian derivative of  $\mathcal{P}_1(\Omega)$  at  $\Omega$  in the direction  $\boldsymbol{\theta}$  is

$$\mathcal{P}'_1(\Omega; \boldsymbol{\theta}) := \lim_{t \rightarrow 0^+} \frac{\mathcal{P}_1(\Omega_t) - \mathcal{P}_1(\Omega)}{t} = \int_{\Omega} \operatorname{div} \boldsymbol{\theta} \, dx, \quad (45)$$

Combined with Theorem 3.7 and 3.9, the Eulerian derivative of the augmented Lagrangian functional in boundary formula is given by

$$d\mathcal{L}_S(\Omega; \boldsymbol{\theta}) = dJ_S(\Omega; \boldsymbol{\theta}) + \int_{\partial\Omega} \left[ \ell + \beta(\mathcal{P}_1(\Omega) - \mathcal{C}_1) \right] \boldsymbol{\theta}_n \, ds, \quad (46)$$

or the distributed Eulerian derivative gives

$$d\mathcal{L}_V(\Omega, \boldsymbol{\theta}) = dJ_V(\Omega; \boldsymbol{\theta}) + \int_{\Omega} \left[ \ell + \beta(\mathcal{P}_1(\Omega) - \mathcal{C}_1) \right] \operatorname{div} \boldsymbol{\theta} \, dx. \quad (47)$$

The initial guess for Lagrange multiplier  $l_0$  should be well chosen because if the value is too small, then the volume constraint is hard to satisfy; on the other hand, large number of multiplier will cause huge oscillation of volume size. In our paper, the initial multiplier is approximated from the first order optimality by taking deformation field with unit outward normal  $\boldsymbol{\theta} = \mathbf{n}$  that

$$l_0 = -\frac{d\mathcal{L}_S(\Omega; \mathbf{n})}{\int_{\partial\Omega} 1 \, ds}. \quad (48)$$

Then a Uzawa type updating scheme for the multiplier reads:

$$l \leftarrow l + \beta(\mathcal{P}_1(\Omega) - \mathcal{C}_1).$$

## 4.2 Shape gradient algorithm

The descent direction can be obtained by solving the  $H^1$  shape gradient descent flow (see [9]) with distributed shape gradient: find  $\boldsymbol{\zeta} \in \mathbf{H}^1(\Omega)$  such that

$$\int_{\Omega} \epsilon_0 D\boldsymbol{\zeta} : D\boldsymbol{\theta} + \boldsymbol{\zeta} \cdot \boldsymbol{\theta} \, dx = -d\mathcal{L}(\Omega; \boldsymbol{\theta}) \quad \forall \boldsymbol{\theta} \in \mathbf{H}^1(\Omega), \quad (49)$$

where  $\mathcal{L} = \mathcal{L}_V$  (or  $\mathcal{L}_S$ ) corresponds to volume (or surface) type of Eulerian derivative and  $\epsilon_0 > 0$  is a diffusion parameter. During grid moving of shape gradient algorithm, the mesh may have low quality even the initial mesh are quasi-uniform. One strategy for improving mesh quality is to use uniform remeshing. Sometimes, the remeshing technique by the Delaunay triangulation is costly in very fine mesh. For 2d space, we can use a special moving mesh method by virtue of conformal transformations (CT) [19] to preserve the angles of triangles during the optimization process. More precisely, denote

$$\mathcal{B} := \begin{pmatrix} -\partial_x & \partial_y \\ \partial_y & \partial_x \end{pmatrix}$$

and the symmetric part of  $D\mathbf{u}$

$$\operatorname{sym}(D\mathbf{u}) := \frac{1}{2} (D\mathbf{u} + D\mathbf{u}^T).$$

Consider a CT+H(sym)-gradient flow that: find  $\boldsymbol{\zeta} \in H^1(\Omega)^2$  such that

$$\int_{\Omega} \frac{1}{\alpha} \mathcal{B}\boldsymbol{\zeta} \cdot \mathcal{B}\boldsymbol{\theta} + \operatorname{sym}(D\boldsymbol{\zeta}) : \operatorname{sym}(D\boldsymbol{\theta}) + \boldsymbol{\zeta} \cdot \boldsymbol{\theta} \, dx = -d\mathcal{L}(\Omega; \boldsymbol{\theta}) \quad \forall \boldsymbol{\theta} \in H^1(\Omega)^2, \quad (50)$$

where  $\alpha > 0$  is penalty parameter to control the effect of CT. Now we are prepared to present the shape gradient algorithm to seek optimal domain of interest meanwhile maintain the quasi-uniformity and regularity of the mesh during shape evolution.

---

**Algorithm 1** Shape gradient algorithm for maximizing ionic concentration

---

**Require:** Choose initial domain  $\Omega_0(k=0)$  and max iteration number  $N_{\max}$

**while**  $k \leq N_{\max}$  **do**  
  Step 1: Solve the PNP system;  
  Step 3: Solve the adjoint system;  
  Step 3: Calculate decent direction via the gradient flow;  
  Step 4: Update the Lagrange multiplier;  
  Step 5: Domain deformation;  
   $k = k + 1$   
**end while**

---

## 5 Numerical schemes

In this section, we consider finite element method to discretize both the state and adjoint variables, as well as the decent directions.

### 5.1 Finite element discretization

Consider a family of quasi-uniform triangulation  $\{\mathcal{T}_h\}_{h>0}$  of  $\Omega$  into triangles/tetrahedrons satisfying  $\Omega_h = \bigcup_{K \in \mathcal{T}_h} \bar{K}$ , where the mesh size  $h := \max_{K \in \mathcal{T}_h} h_K$  with  $h_K$  being the diameter of any  $K \in \mathcal{T}_h$ . Suppose that the discrete domain  $\Omega_h$  corresponding to the continuous domain  $\Omega$  be a polygon. Let us consider the conforming finite subspaces characterized by the discrete function space  $W_h \subset H^1(\Omega)$  where  $W_h$  denotes the piece-wise linear polynomial space  $W_h = \{q_h \in C^0(\Omega_h) \mid q_h|_K \in \mathbb{P}_1, \forall K \in \mathcal{T}_h\}$ . A triangulation is strongly acute [27] if the sum of opposite angles to each common side/face of adjacent triangles is  $\leq \pi - \theta$ , with  $\theta > 0$  independent of mesh size  $h$ . Obtaining a satisfactory numerical solution of the PNP (1) is challenging especially when the convection dominates the diffusion. In next subsection, we will introduce the so-called Gummel [15] map, a nonlinear block iterative algorithm that splits PNP system (1) into a self-adjoint Poisson equation for the electric potential and continuity system for concentration. For solving PNP (1) numerically, consider both potential and concentration discretized by piece-wise linear polynomials. We introduce the slotboom transformation [5] for the concentration function

$$c_{i,h} = \rho_{i,h} \exp(-z_i \phi_h),$$

then the Maxwell-Boltzmann statistics becomes  $\sum_{i=1}^N z_i \rho_{i,h} \exp(-z_i \phi_h)$ . Denote the discrete function space  $W_{g,h} := \{q_h \in W_h \mid q_h = g \text{ on } \Gamma_2\}$  for discrete potential, the vectorial discrete space  $\mathbf{W}_h := (W_h)^N$ , and the vectorial discrete space  $\mathbf{W}_{\rho,h} := \{\boldsymbol{\rho}_h \in (W_h)^N \mid \rho_{i,h} = c_i^\infty \exp(z_i \phi_h) \text{ on } \Gamma_{\text{in}}\}$  for slotboom variable of the concentration where  $\boldsymbol{\rho}_h = [\rho_{1,h}, \rho_{2,h}, \dots, \rho_{N,h}]^T$ . Denote the discrete function spaces  $\mathbf{W}_{0,h} := \{\mathbf{w}_h \in \mathbf{W}_h, w_h = 0 \text{ on } \Gamma_{\text{in}}\}$  and  $W_{0,h} := \{w_h \in W_h, w_h = 0 \text{ on } \Gamma_2\}$  for the discrete adjoint variables. Then the discrete system of PNP (1) is given by: find  $(\boldsymbol{\rho}_h, \phi_h) \in \mathbf{W}_{\rho,h} \times W_{g,h}$  such that

$$\begin{cases} \int_{\Omega} \exp(-z_i \phi_h) \nabla \rho_{i,h} \cdot \nabla v_{i,h} dx = 0, & \forall \mathbf{v}_h \in \mathbf{W}_h, \\ \int_{\Omega} \epsilon \nabla \phi_h \cdot \nabla \zeta_h dx = \int_{\Omega} \left( \sum_{i=1}^N z_i \rho_{i,h} \exp(-z_i \phi_h) \right) \zeta_h dx, & \forall \zeta_h \in W_h, \end{cases} \quad (51)$$

where the vectorial test function gives  $\mathbf{v}_h = [v_{1,h}, v_{2,h}, \dots, v_{N,h}]^T$ . The discrete PNP system (51) incorporating the nonlinear term, to solve it numerically and efficiently, we introduce the Gummel fixed-point method [15] preserving good convergence properties (even in case of a badly chosen initial guess). Set the initial concentration functions and stopping parameter  $\tau > 0$ . Then the Gummel fixed-point scheme [5] are given by the following four steps:

**Gummel fixed-point scheme for steady-state Poisson-Nernst-Planck system:**

*Step 1:* Check whether the stopping criterion is acceptable  $\|\phi_h^{\ell+1} - \phi_h^\ell\|_1 \leq \tau$  and  $\|\boldsymbol{\rho}_h^{\ell+1} - \boldsymbol{\rho}_h^\ell\|_1 \leq \tau$ . If true, then output the solution  $(\boldsymbol{\rho}_h^{\ell+1}, \phi_h^{\ell+1})$ ; Otherwise, continue to *Step 2*.

*Step 2:* Solve the semi-linear Poisson equation for potential  $\phi_h^{\ell+1} \in W_{g,h}$  such that

$$\int_{\Omega} \epsilon \nabla \phi_h^{\ell+1} \cdot \nabla \zeta_h dx = \int_{\Omega} \left( \sum_{i=1}^N z_i \rho_{i,h}^\ell \exp(-z_i \phi_h^{\ell+1}) \right) \zeta_h dx, \quad \forall \zeta_h \in W_h. \quad (52)$$

*Step 3:* Solve decoupled continuity system  $\boldsymbol{\rho}_h^{\ell+1} \in \mathbf{W}_{\rho,h}$  such that

$$\int_{\Omega} \exp(-z_i \phi_h) \nabla \rho_{i,h} \cdot \nabla v_{i,h} dx = 0, \quad \forall \mathbf{v}_h \in \mathbf{W}_h. \quad (53)$$

*Step 4:* Update  $\ell = \ell + 1$  and go back to *Step 1*.

The convergence property [22, page 332] for Gummel fixed-point scheme in continuous functional space is guaranteed. Noticing that the semi-linear Poisson equation (52) can be solved efficiently by Newton iteration which preserves the quadratic convergence rate locally. Define the mapping  $\mathcal{F} : H^1(\Omega) \rightarrow H^{-1}(\Omega)$  such that

$$\mathcal{F}(\phi, \zeta) = \int_{\Omega} \epsilon \nabla \phi \cdot \nabla \zeta - \left( \sum_{i=1}^N z_i \rho_i \exp(-z_i \phi) \right) \zeta \, dx, \quad \forall \zeta \in H^1(\Omega). \quad (54)$$

Hence the semi-linear Poisson equation (52) is equivalent to find  $\phi \in H_{\Gamma_2, d}^1(\Omega)$  such that  $\mathcal{F}(\phi, \zeta) = 0$ .

**Newton's method in inner iteration for solving semi-linear Poisson equation:**

(i) Output the potential function if increment  $\delta_\phi$  is small enough; Otherwise continue to (ii).

(ii) Find the decent direction  $\delta_\phi \in H^1(\Omega)$  such that  $D\mathcal{F}(\phi_n^\ell)(\delta_\phi) = -\mathcal{F}(\phi_n^\ell)$ , where  $D\mathcal{F}(\phi_n^\ell)$  is the Jacobian of  $\mathcal{F}$  at  $\phi_n^\ell$ .

(iii) Update the solution by  $\phi_{n+1}^\ell = \phi_n^\ell + \tau_0 \delta_\phi$  for a suitable step size  $\tau_0$  and go back to (i).

We approximate the exponential coefficient  $\exp(\phi)$  (respectively  $\exp(-\phi)$ ) with the piecewise constant  $E(\phi)_K$  (respectively  $E(-\phi)_K$ ) on each unit  $K \in \mathcal{T}_h$ . Then the discrete form of continuity equation (53) becomes

$$0 = \sum_{K \in \mathcal{T}_h} \int_K \exp(-z_i \phi_h) \nabla \rho_{i,h} \cdot \nabla v_{i,h} \, dx \approx \sum_{K \in \mathcal{T}_h} E(-z_i \phi_h)_K \int_K \nabla \rho_{i,h} \cdot \nabla v_{i,h} \, dx. \quad (55)$$

The  $\exp(\phi)$  and  $\exp(-\phi)$  can be approximated by the averaging techniques [6, 33] over the whole unit  $K$ , that is  $E(\phi)_K$  (respectively  $E(-\phi)_K$ ) being a constant on each tetrahedral/triangle unit. Using the harmonic average to treat singular coefficients which has been proven to be able to provide a better result than the general mean value in the one-dimensional case, especially when the singular coefficient exhibits sharp variations or is even discontinuous on mesh elements. Thus we approximate the exponential coefficients with their respective harmonic averaging over the whole element  $K$  as follows

$$E(\phi)_K = \left( \frac{1}{|K|} \int_K \exp(-\phi) \, dx \right)^{-1}. \quad (56)$$

If the triangulation  $\mathcal{T}_h$  is of weakly acute type, then the matrix associated with (55) is an M-matrix [6] exhibiting good property for conservation and non-negativity. For 2d space, the exponential fitting method is performed under every triangular unit on triangulation mesh. Meanwhile for 3d space, this harmonic averaging technique is computed on every tetrahedron of the tetrahedral mesh.

## 5.2 Discrete adjoint problem

The finite element discretization of the adjoint problem (5) is to find  $\mathbf{s}_h = [s_{1,h}, s_{2,h}, \dots, s_{N,h}]^T \in \mathbf{W}_{0,h}$  and  $\psi_h \in W_{0,h}$  such that for all  $(\mathbf{v}_h, \zeta_h) \in \mathbf{W}_h \times W_h$

$$\begin{cases} \int_{\Omega} \nabla s_{i,h} \cdot \nabla v_{i,h} + z_i \nabla \phi_h \cdot \nabla s_{i,h} v_{i,h} - z_i \psi_h v_{i,h} + j'(c_{i,h}) v_{i,h} \, dx = 0, \\ \int_{\Omega} \epsilon \nabla \psi_h \cdot \nabla \zeta_h \, dx = - \int_{\Omega} \left( \sum_{i=1}^N z_i c_{i,h} \nabla s_{i,h} \right) \cdot \nabla \zeta_h \, dx. \end{cases} \quad (57)$$

The adjoint system in discretized form (57) can be transformed into linear algebraic system. Let  $\mathcal{N}_h$  be the set of all nodes in  $\mathcal{T}_h$  and  $\{q\}_{i=1}^{|\mathcal{N}_h|}$  be the elements in  $\mathcal{N}_h$ . The nodal interpolation operator  $\mathcal{I}_h : C(\Omega_h) \rightarrow W_h$  such that for all  $\omega \in C(\Omega_h)$  we have  $\mathcal{I}_h \omega = \sum_{q \in \mathcal{N}_h} \omega(q) \nu_q$  where  $\nu_q \in W_h$  denotes the nodal basis. Suppose the state variables are given by the linear combination of the nodal basis with  $s_h = \sum_{q \in \mathcal{N}_h} s_q \nu_q$  and  $\psi_h = \sum_{q \in \mathcal{N}_h} \psi_q \nu_q$ . Denote the vector of right-hand side  $(F_k)_i = (-j'(c_{k,h}), \nu_{q_i})$  where  $k = 1, 2, \dots, N$ . Denote the following matrices that stiffness matrix  $(A)_{i,j} = (\nabla \nu_{q_i}, \nabla \nu_{q_j})$ , mass matrix  $(B)_{i,j} = (\nu_{q_i}, \nu_{q_j})$ , unsymmetric matrix  $(C)_{i,j} = (\nabla \phi_h \cdot \nabla \nu_{q_i}, \nu_{q_j})$  and  $(D_k)_{i,j} = (c_{k,h} \nabla \nu_{q_i}, \nabla \nu_{q_j})$ . By the Galerkin orthogonality, the algebraic system of (57) is: find vectors  $S_1, S_2, \dots, S_N \in \mathbb{R}^{|\mathcal{N}_h|}$  and  $\Psi \in \mathbb{R}^{|\mathcal{N}_h|}$  such that

$$\left[ \begin{array}{cccc|c} A + z_1 C & \mathbf{0} & \cdots & \mathbf{0} & -z_1 B \\ \mathbf{0} & A + z_2 C & \cdots & \mathbf{0} & -z_2 B \\ \vdots & \vdots & \ddots & \vdots & \vdots \\ \mathbf{0} & \mathbf{0} & \cdots & A + z_N C & -z_N B \\ \hline z_1 D_1 & z_2 D_2 & \cdots & z_N D_N & \epsilon A \end{array} \right] \begin{pmatrix} S_1 \\ S_2 \\ \vdots \\ S_N \\ \Psi \end{pmatrix} = \begin{pmatrix} F_1 \\ F_2 \\ \vdots \\ F_N \\ \mathbf{0} \end{pmatrix}, \quad (58)$$

with each undetermined vector  $S_k = [s_1, s_2, \dots, s_{|\mathcal{N}_h|}]^T$  ( $k = 1, 2, \dots, N$ ) and  $\Phi = [\phi_1, \phi_2, \dots, \phi_{|\mathcal{N}_h|}]^T$ .



### 5.3 Discrete shape gradient flow

We use Galerkin linear finite element method to discretize  $H^1$  gradient flow (49) as well as CT gradient flow (50). The discrete descent direction for  $H^1$  gradient flow is given by: find  $\zeta_h \in \mathbf{W}_h$  such that

$$\int_{\Omega} \epsilon_0 D\zeta_h : D\theta_h + \zeta_h \cdot \theta_h = -d\mathcal{L}(\Omega_h; \theta_h) \quad \forall \theta_h \in \mathbf{W}_h. \quad (59)$$

The linear system after discretization can be efficiently solved by the conjugate gradient method since each coefficient matrix is symmetric and positive definite. The vector-field gradient flow can be decomposed into  $d$  scalar system for fast numerical computation especially for 3d space. The vectorial  $H^1$  shape gradient flow is equivalent to scalar  $H^1$  shape gradient flows [21]: Find  $\zeta_{i,h} \in W_h$  ( $i = 1, \dots, d$ ) such that

$$\int_{\Omega} \epsilon_0 \nabla \zeta_{i,h} \cdot \nabla \eta_h + \zeta_{i,h} \eta_h = -d\mathcal{L}(\Omega_h; \xi_h^i) \quad \forall \eta_h \in W_h, \quad (60)$$

where  $\xi_h^i = [0, \dots, \eta_h, \dots, 0]^T$  with  $\eta_h$  locating at the  $i$ -th component. The discrete CT+H(sym)-gradient flow in 2d space is given by: find  $\zeta_h \in (W_h)^2$  such that

$$\int_{\Omega} \frac{1}{\alpha} \mathcal{B}\zeta_h \cdot \mathcal{B}\theta_h + \text{sym}(D\zeta_h) : \text{sym}(D\theta_h) + \zeta_h \cdot \theta_h = -d\mathcal{L}(\Omega_h; \theta_h) \quad \forall \theta_h \in (W_h)^2. \quad (61)$$

Let  $\Omega_{h,k}$  ( $k = 0, 1, 2, \dots$ ) denote the mesh at the  $k$ -th iteration. After the discrete decent direction  $\zeta_{k,h}$  is computed, we can move meshes. The grid is updated by

$$\Omega_{h,k+1} = (\mathbb{I} + \delta_k \zeta_{k,h}) \Omega_{h,k},$$

where  $\mathbb{I}$  denotes the identity operator and  $\delta_k > 0$  is a suitable step size.

## 6 Numerical experiments

Numerical simulations are performed with FreeFem++ [18] on a computer with Intel Core i7-7820x @3.60 GHz and RAM 16.0 GB. In this section, we test numerical performance of the algorithm with several shape design examples.

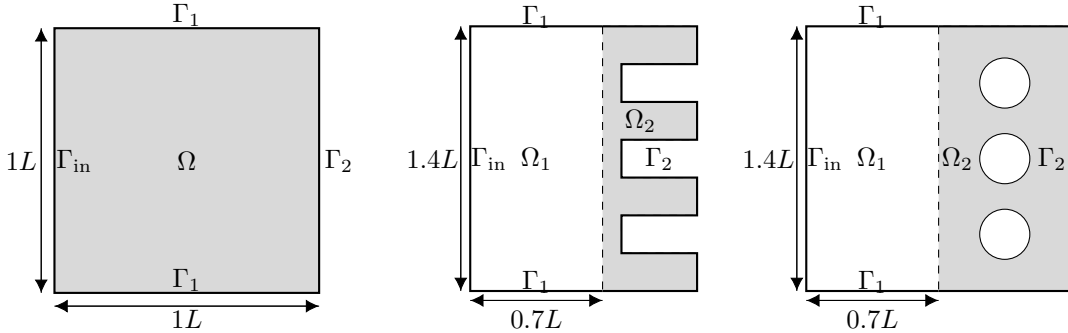


Figure 2: Illustrations for regions: square domain (left), irregular domain (middle) and porous domain (right).

### 6.1 Shape design in 2d space

In this subsection, we use several gradient flows to perform numerical experiment. For verifying the effectiveness of shape gradient algorithms on different topologies of domain, we test numerical examples on regular, irregular and porous regions in 2d case (see Fig. 2). Let the gray shaded sub-region be the design domain where the total weighted concentration is calculated. Take  $L = 1$  for all the cases except for some exceptions. To prevent the profile from exceeding the range in  $y$ -axis, a Sigmoid type of filter is considered with deformation vanishing along the vertical direction on the edges, i.e.

$$\mathcal{S}(y) = \begin{cases} \frac{1}{1 + \exp(-M(y - y_{\min}))}, & y < \frac{y_{\min} + y_{\max}}{2}, \\ \frac{1}{1 + \exp(M(y - y_{\max}))}, & y \geq \frac{y_{\min} + y_{\max}}{2}, \end{cases} \quad (62)$$

where  $M$  is a sufficiently large number and  $y_{\min}$  and  $y_{\max}$  denote lower and upper limits of the computational domain along y-axis, respectively. After the decent direction  $\zeta_{i,h}$  ( $i = 1, 2$ ) computed, we replace  $\zeta_{2,h}$  by  $\zeta_{2,h} = \mathcal{S}(y)\zeta_{i,h}(x, y)$ . Take  $M = 100$  for all experiments. Fix the dielectric coefficient  $\epsilon = 1.0$  for all 2d cases. For preventing the mesh from twisting and emerging especially for irregular domain, the perimeter regularization  $\frac{1}{2}\gamma|\partial\Omega|^2$  is considered adding to the objective with small parameter  $\gamma \ll 1$ .

**Experiment 1 (Square domain):** Consider maximization of the ionic concentration on a regular square domain (see Fig. 2 left).

**Case 1.1.** Consider only one ionic species and test Algorithm 1 with boundary type of shape gradient first. The setting of the Dirichlet boundary condition is given by  $c^\infty = 1$  on  $\Gamma_{\text{in}}$  with valence  $z = 1$  and  $\phi = -0.75$  on  $\Gamma_2$ . Set the initial domain be the square (see line 1 left of Fig. 3) with volume of  $|\Omega| = 1$ . The initial mesh has 5938 triangular units. The target volume is  $\mathcal{C}_1 = 1.75$ , perimeter penalty coefficient  $\gamma = 1e-4$  and  $\epsilon_0 = 0.05$ . Denote by  $N_e$  the number of mesh elements of initial mesh. We assume that each triangle of the initial mesh is equilateral so that we compute numerically the mesh characteristic length  $\sqrt{4\text{meas}(\Omega)/(\sqrt{3}N_e)}$  which is used for regular and quasi-uniform remeshing in FremFem++ [9]. In Fig. 3, the optimal mesh shape computed by boundary type of  $H^1$  gradient flow is presented with two corners protruding. See Fig. 3 for contours of concentration, potential and electric field corresponding to the optimized design. We find that positive ions gather at the right edge and the concentration of positive ionic species increases along the direction of electric field.

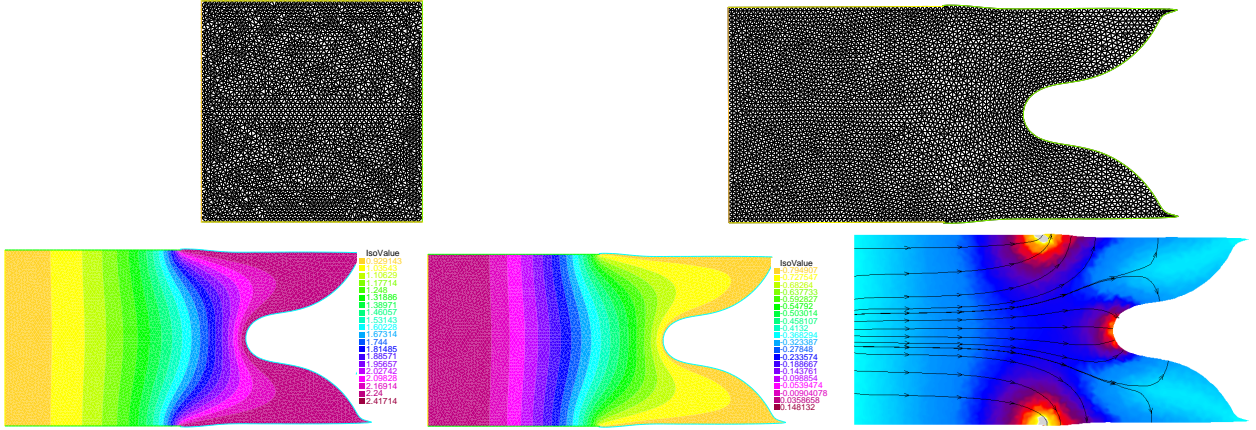


Figure 3: Initial and optimized designs (left and right on line 1), concentration, potential and electric fields (left, middle, right on line 2) for case 1.1.

**Case 1.2.** Fixing the parameter  $\alpha = 2$ , test the CT gradient flow (50) for the same boundary conditions and optimization parameters as the above. For CT gradient flow preserving the angles in every triangular unit, the optimized shape seems to be smoother while the objective is almost close to that calculated by  $H^1$  gradient flow (see Fig. 4). The optimized design, its corresponding contours of concentration and potential by CT-H(sym) gradient flow (50) are presented in Fig. 4 (line 1). From Fig. 4 (line 2), we see that the convergence histories of the objective tend to be flat and the volume errors amount to  $1e-2$  for both  $H^1$  and CT-H(sym) gradient flows with boundary type of shape gradient.

**Case 1.3.** In this case, test CT gradient flow with shape gradient in domain expression with relatively coarse mesh. Choosing the same initial shape, set volume target  $\mathcal{C}_1 = 1.3$ . Other boundary conditions and optimization parameters are the same as the above. In Fig. 5, the optimized domain is shown similar to CT gradient flow with boundary type of shape gradient. The convergence histories are presented to show the effectiveness of the optimization algorithm by shape gradient in domain expression.

The numerical experiments are performed by gradient flows with boundary type of shape gradient in the following experiments.

**Case 1.4.** Now consider two kinds of ionic species ( $N = 2$ ) with positive ion and negative ion. Take the following parameters  $c_1^\infty = 0.5$  with  $z_1 = 1$ ,  $c_2^\infty = 0.5$  with  $z_2 = -1$  and  $g = -0.5$ . Set volume target  $\mathcal{C}_1 = 1.3$ , penalty parameter  $\beta = 2$ . The initial domain is a unit square and the same triangulation as Case 1.1 is used. In the first line of Fig. 6, the optimized design and its velocity field are presented. In the second line of Fig. 6, we see that the concentration of positive ionic species accumulate at the right edge while the concentration while the concentration of the negative ionic species is rare on the right part of the domain. The convergence histories for both objective and volume error are presented in the third line showing the effectiveness of the optimization algorithm we proposed.

**Experiment 2 (Irregular domain):** In this experiment, we choose the initial domain as an irregular shape (see Fig. 2 middle). The objective is defined on a subdomain by  $J(\Omega_2) = \int_{\Omega_2} \tilde{j}(c) dx$ . The shape sensitivity

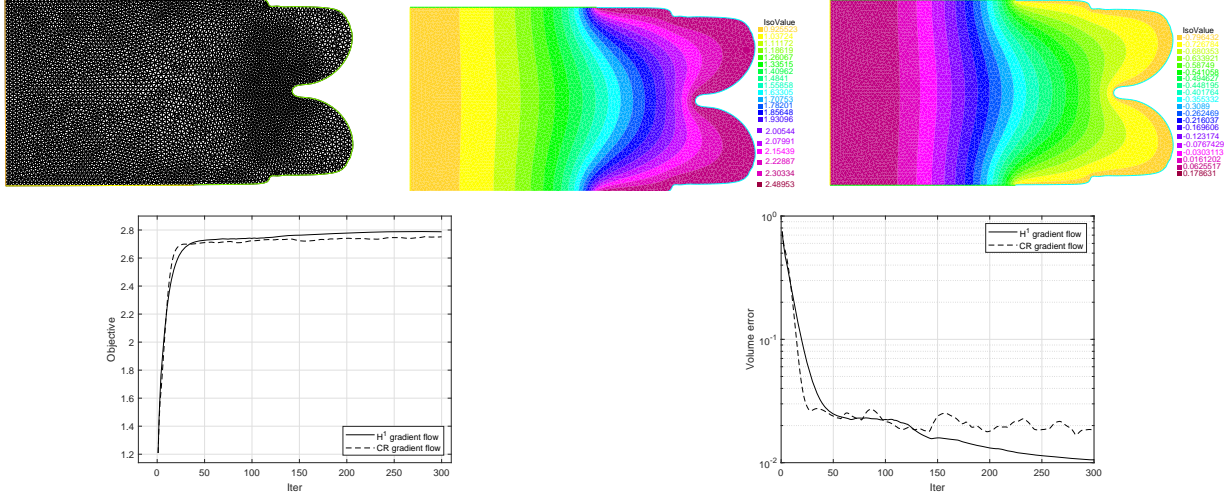


Figure 4: Optimal mesh, concentration, potential (left, middle, right on line 1) for case 1.2, the convergence histories of objective and volume error (left, right on line 2) for case 1.1 and 1.2.

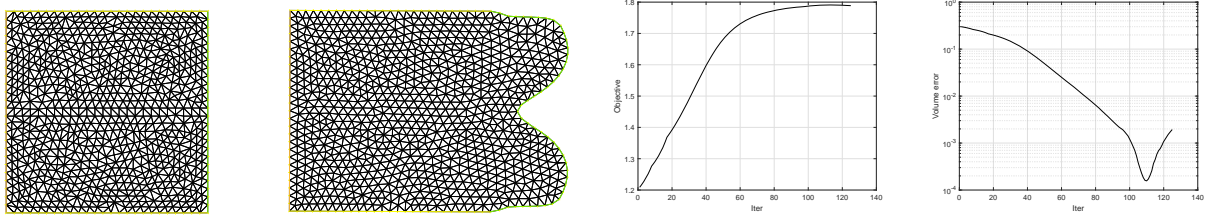


Figure 5: Initial (first), optimal mesh (second), convergence histories of objective (third) and volume error (fourth) for case 1.3.

analysis is almost the same except right-hand side term in adjoint system (5) is replaced by  $-\chi_{\Omega_2} j'(c_i)$  where

$$\chi_{\Omega_2} = \begin{cases} 1, & \text{in } \Omega_2, \\ 0, & \text{in } \Omega \setminus \Omega_2. \end{cases} \quad (63)$$

Shape evolution is performed by CT gradient flow with boundary type of shape gradient (50).

**Case 2.1.** Firstly, maximize one kind of concentration with positive ionic species by setting  $c^\infty = 0.5$ ,  $z = 1$ ,  $\gamma = 0.1$ ,  $g = -0.5$  and  $C_1 = 1.5$ . The initial design, optimized design and electric field are shown on line 1 of Fig. 7. From line 2 of Fig. 7, we see that the positive ion accumulates in the right part of the domain  $\Omega_2$ . From the optimized shape, the four irregular pockets are expanded outward as much as possible to accommodate more ion implantation. Among the four pockets, the effect of electric field force is almost zero, and the ions stay inside are in a relatively stationary state. See line 3 for convergence histories of objective and volume error.

**Case 2.2.** Next, consider both positive and negative ionic species  $c_i$  ( $i = 1, 2$ ) with its valence  $z_1 = 1$  and  $z_2 = -1$ . Set the boundary condition for concentration function on  $\Gamma_{\text{in}}$  with  $c_1^\infty = 0.5$  and  $c_2^\infty = 0.5$ , respectively. Set the boundary condition for potential on  $\Gamma_2$  that  $g = -1.0$ . Set parameters  $\gamma = 0.2$ ,  $\alpha = 2.5$ ,  $\beta = 5$  and  $C_1 = 1.6$ . The other settings are the same as *Case 2.1*. The results shown in Fig. 8, we see that the positive ionic species accumulates in the finger-shaped domain  $\Omega_2$  while the concentration of negative ionic species is rare in the same area.

**Case 2.3.** For last case, consider the wavy initial boundary by parameterized curve

$$\Gamma_2 = \{(x, y) | x = 0.4 + 0.05 \sin(55/7\pi t), y = t, t \in [0, 1.4]\}.$$

Set the length of  $\Gamma_1$  as 0.4 while the length of  $\Gamma_{\text{in}} = 1.4$ . The boundary conditions are the same as case 2.1 for taking only one kind of positive ionic species for consideration. The volume target is 1.5 times of the initial volume. Set  $\beta = 5.0$ ,  $\gamma = 1e - 3$  and  $\alpha = 2.5$ . The initial mesh is partitioned into 19976 unit triangles and 10339 vertices with refinement on the right edge (see Fig. 9 left 1). The corresponding concentration, potential and electric field are presented in Fig. 9 for the rest sub-figures. See Fig. 10 for the convergence histories of the objective value and volume error. Notice that in this case, a suitable parameter  $\gamma$  is indispensable to prevent

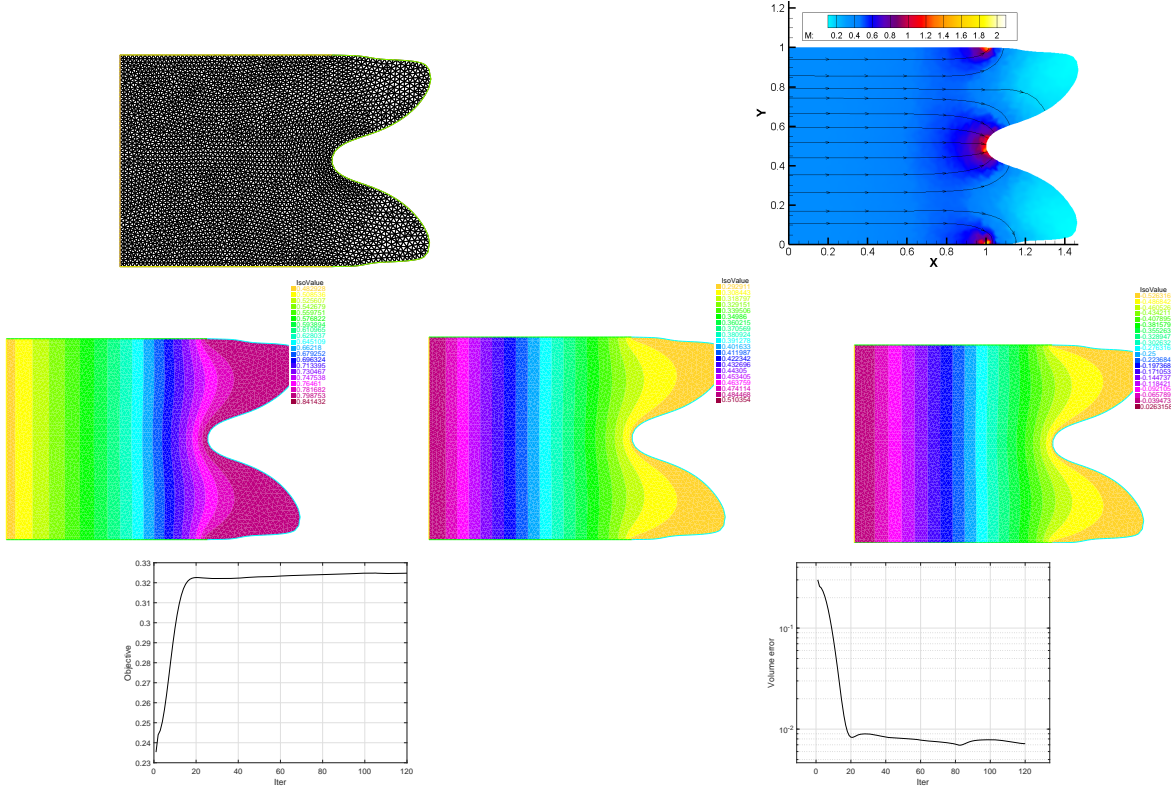


Figure 6: Optimal mesh (left, line 1), electric field (right, line 1), concentration  $c_1$  (left, line 2), concentration  $c_2$  (middle, line 2), potential (right, line 2), convergence histories of objective (left, line 3) and volume error (right, line 3) for case 1.4.

the curves overlapping. On the other hand, excessive value of  $\gamma$  makes the curve too smooth and difficult to obtain complicated geometric structures.

**Experiment 3 (Porous domain):** Let the initial domain be porous region with three irregular shapes inside (see Fig. 2 right) simulating some impurities mixed in the object. The boundary condition around the holes is considered by homogeneous Neumann condition for both concentration and potential functions.

**Case 3.1.** Firstly, maximize one kind of the concentration with positive ionic species by setting  $c^\infty = 0.5$ ,  $z = 1$  and  $g = -0.5$ . Set parameters  $\gamma = 10^{-3}$ ,  $\alpha = 2.5$  and  $\beta = 5.0$ . The volume target is 1.25 times of the initial volume. The initial mesh (8666 triangular units), optimal mesh and electric field are shown in Fig. 11 line 1. From line 2 of Fig. 11, we see that the positive ion accumulates in the right part of the domain  $\Omega_2$ . See line 3 on the same figure for convergence histories of objective and volume error.

**Case 3.2.** Consider both positive and negative ionic species  $c_i$  ( $i = 1, 2$ ) with its valence  $z_1 = 1$  and  $z_2 = -1$ . Test for another three holes randomly generated in the initial domain. Boundary conditions and volume target are the same as above. Set parameters  $\gamma = 10^{-3}$ ,  $\alpha = 2.5$  and  $\beta = 5$ . The results of optimal mesh, electric field, concentration, potential and convergence histories are shown in Fig. 12. We see that the positive ion accumulates in the domain  $\Omega_2$  while the concentration of negative ionic species is rare in domain  $\Omega_2$ .

## 6.2 Shape design in 3d space

In this subsection, consider shape optimization for maximizing the ionic concentration in 3d space. However, CT gradient flow (61) is only available in 2d space. For accelerating the efficiency of the optimization, utilize scalar  $H^1$  gradient flow (60) to obtain the decent direction. Fix the dielectric coefficient  $\epsilon = 0.5$  for all the 3d cases.

**Experiment 4 (Irregular domain in 3d):**

**Case 4.1.** The computational domain is considered in irregular domain (see Fig. 13). Consider only one kind of positive ionic species with  $z = 1$ . Take  $\epsilon = 0.5$ ,  $c^\infty = 0.5$ ,  $g = -0.5$  with only one species, and volume target 1.2 times of initial volume. Set parameters  $\gamma = 2.5 \times 10^{-3}$  and  $\beta = 5$ . The initial mesh with 57344 tetrahedron elements, the corresponding optimal mesh, the contours of the concentration and potential corresponding to the optimal shape are presented in Fig. 14.

**Case 4.2.** Consider two kinds of ionic species with  $z_1 = 1$  and  $z_2 = -1$ . Take larger volume target by 1.4



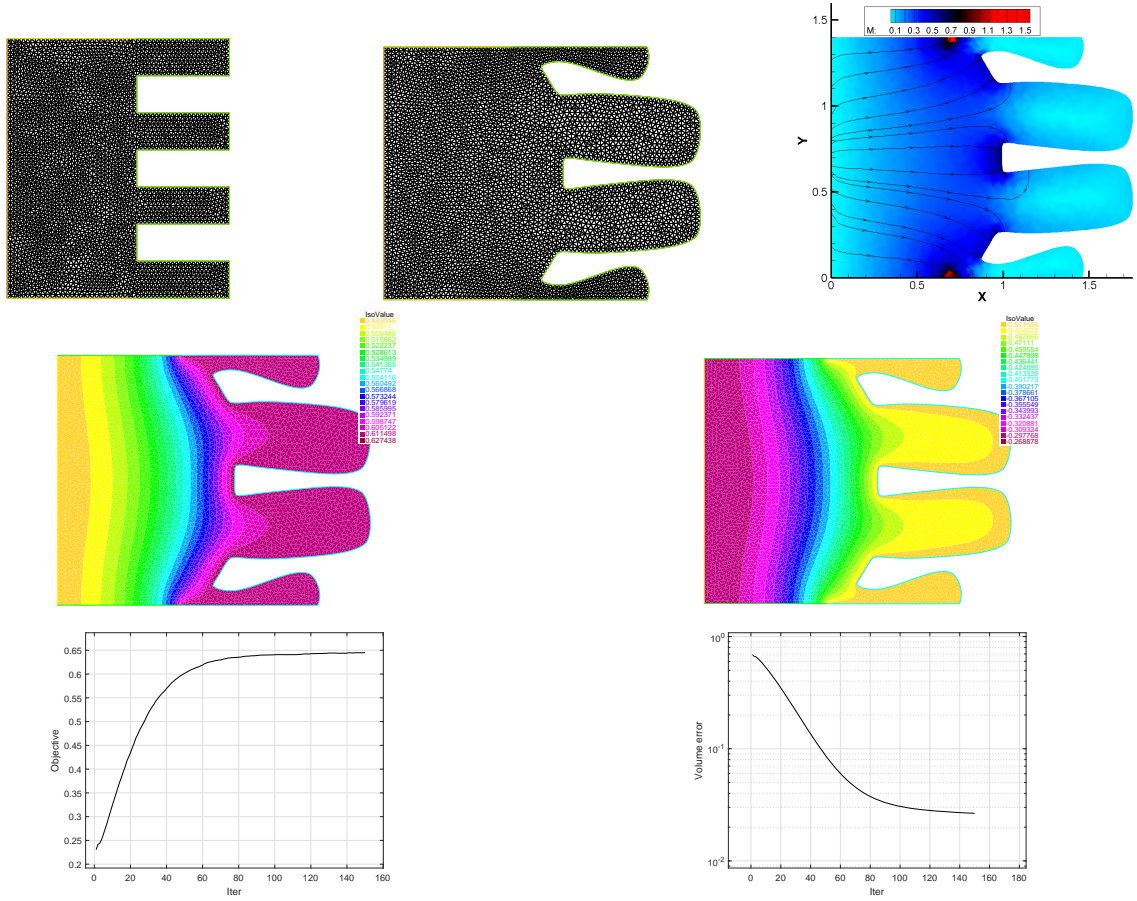


Figure 7: Initial design (left, line 1), optimized design (middle, line 1), electric field (right, line 1), concentration (left, line 2), potential (right, line 2), convergence histories of objective (left, line 3) and volume error (right, line3) for case 2.1.

times of initial volume. The boundary conditions are  $g = -1, c_1^\infty = 0.5, c_2^\infty = 0.5$ . The other parameter are the same as the above. In Fig. 15, the optimal mesh, the corresponding potential, concentration  $c_1$  and  $c_2$  are shown. The convergence histories for both objective and volume error are shown in Fig. 16.

## 7 Conclusion

We build the shape optimization problem to maximize the concentration for ionic species under some geometric volume constraint. Shape sensitivity analysis is used to deduce shape gradients. The Gummel fixed-point method with finite element discretization is considered to solve the PNP system. Numerical experiments of practical use both in 2d and 3d spaces are presented to show the effectiveness of the optimization algorithm proposed.

## References

- [1] G. Allaire and F. Jouve, A level-set method for vibration and multiple loads structural optimization. *Comput. Methods Appl. Mech. Engrg.* 194(30-33), (2005) pp. 3269-3290.
- [2] M. Bazant, K. Thornton and A. Ajdari, Diffuse-charge dynamics in electrochemical systems. *Phys. Rev. E* 70 (2004) 021506.
- [3] M.P. Bendsøe and O. Sigmund, *Topology Optimization: Theory, Methods and Applications*. Springer, 2003.
- [4] D. Bucur and G. Buttazzo, *Variational Methods in Shape Optimization Problems*, Appl. Birkhäuser Boston Inc, Boston, 2005.
- [5] F. Brezzi, L.D. Marini, S. Micheletti, P. Pietra, R. Sacco and S. Wang, Discretization of semiconductor device problems. *Handb. Numer. Anal.*, 13, (2005) pp. 317-441.

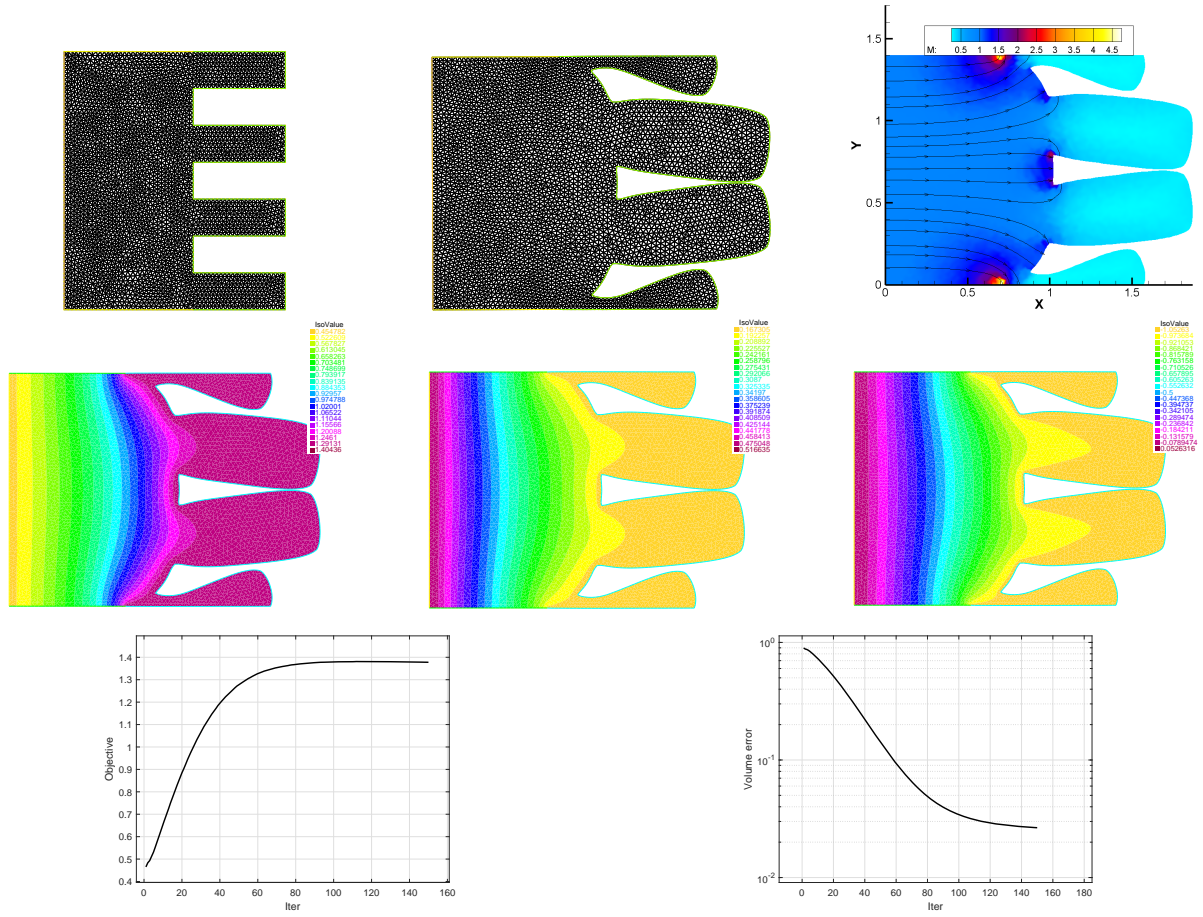


Figure 8: Line 1: Initial (left), optimal meshes (middle), electric field (right); Line 2: concentration  $c_1$  (left), concentration  $c_2$  (middle), potential (right); Line 3: convergence histories of objective (left) and volume error (right) for case 2.2.

- [6] F. Brezzi, L. D. Marini and P. Pietra, Two-dimensional exponential fitting and applications to drift-diffusion models. *SIAM J. Numer. Anal.* 26 (1989) pp. 1342-1355.
- [7] F. Brezzi, L. Marini, P. Markowich and P. Pietra, On some numerical problems in semiconductor device simulation, In: G. Toscani, V. Boffi, S. Rionero (eds) *Mathematical Aspects of Fluid and Plasma Dynamics. Lecture Notes in Mathematics*, vol 1460. Springer, Berlin, Heidelberg, 1991.
- [8] S.J. Cox and D.C. Dobson, Maximizing band gaps in two-dimensional photonic crystals. *SIAM J. Appl. Math.* 59 (1999) pp. 2108-2120.
- [9] C. Dapogny, P. Frey, F. Omnès et al. Geometrical shape optimization in fluid mechanics using FreeFem++. *Struct. Multidisc. Optim.* 58 (2018) pp. 2761-2788.
- [10] M.C. Delfour and J.-P. Zolésio, *Shapes and Geometries: Metrics, Analysis, Differential Calculus, and Optimization*. 2nd ed. SIAM, Philadelphia (2011).
- [11] Y. Deng et.al. Topology optimization of electrode patterns for electroosmotic micromixer. *Int. J. Heat Mass Transf.* 126 (2018) pp. 1299-1315.
- [12] I. Dione, N. Doyon and J. Deteix, Sensitivity analysis of the Poisson Nernst-Planck equations: a finite element approximation for the sensitive analysis of an electrodiffusion model. *J. Comput. Biol.* 78 (2019) pp. 21-56.
- [13] R. Eisenberg, Ion channels in biological membranes: electrostatic analysis of a natural nanotube. *Contemp. Phys.* 39 (1998) 447.
- [14] C. Gardner, W. Nonner and R. Eisenberg, Electrodiffusion model simulation of ionic channels: 1D simulations. *J. Comput. Electron.* 3 (2004) pp. 25-31.

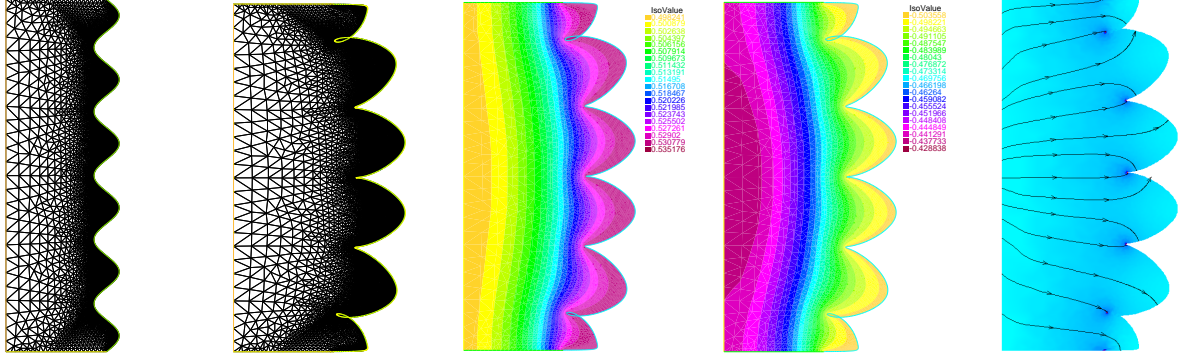


Figure 9: Initial/optimal mesh, concentration, potential and electric field of the optimal shape from left to right for case 2.3.



Figure 10: Convergence histories for objective value and volume error for case 2.3.

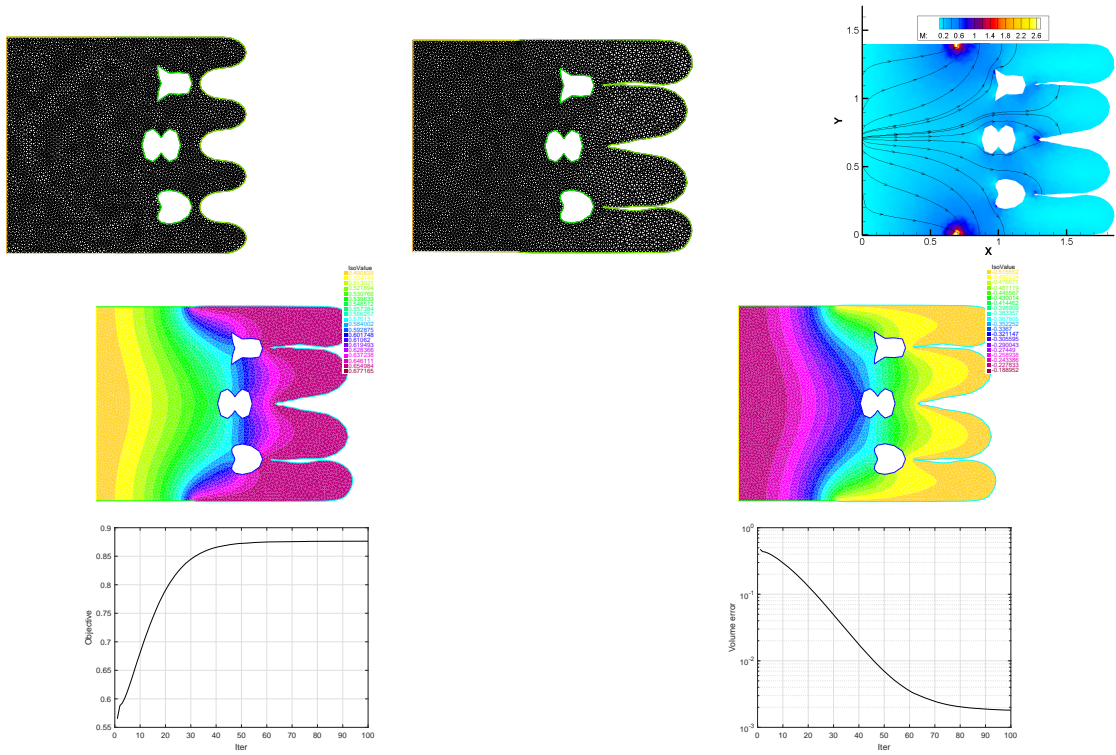


Figure 11: Initial mesh (left, line 1), optimal mesh (middle, line 1), electric field (right, line 1), concentration (left, line 2), potential (right, line 2) corresponding to the optimal shape, objective (left, line 3) and volume error (right, line 3) for case 3.1.



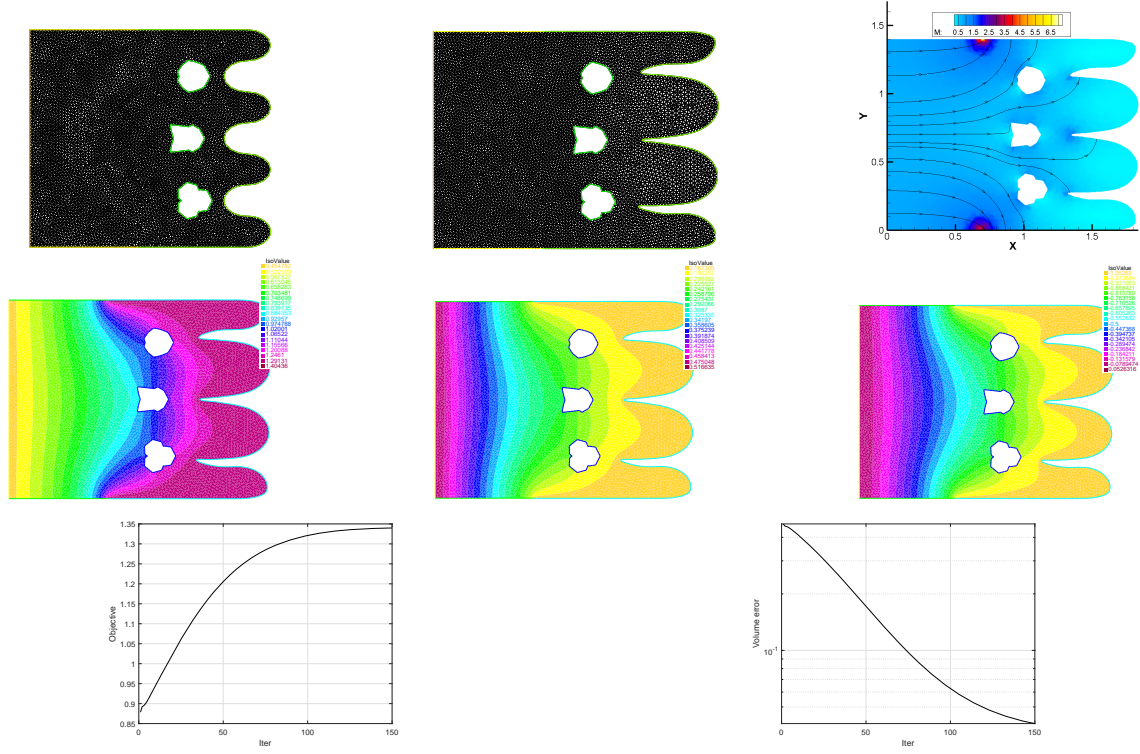


Figure 12: Initial mesh (left, line 1), optimal mesh (middle, line 1), electric field (right, line 1), concentration  $c_1$  (left, line 2),  $c_2$  (middle, line 2), potential (right, line 2), objective (left, line 3) and volume error (right, line 3) for case 3.2.

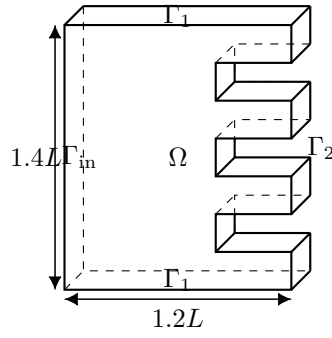


Figure 13: Illustration for computational region in 3d.

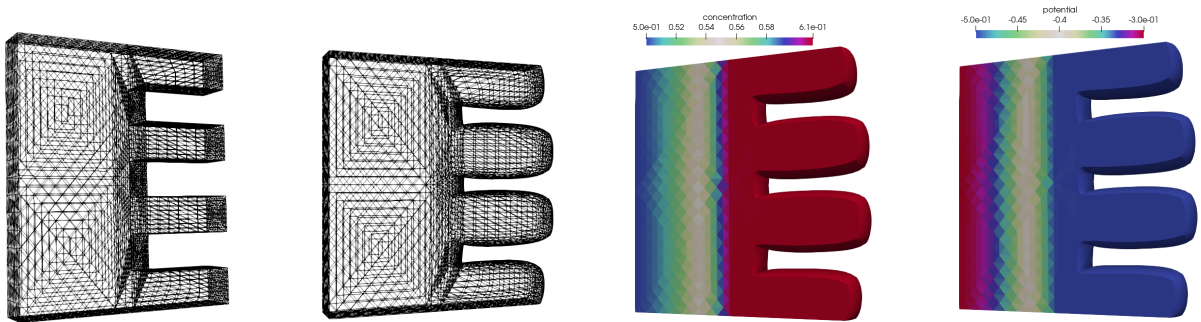


Figure 14: Initial design, optimized design, concentration  $c$ , and potential from left to right for case 4.1.



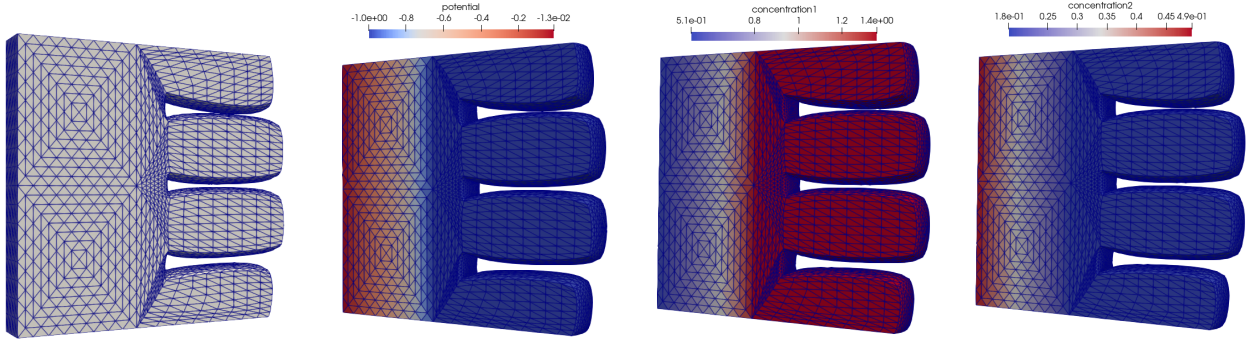


Figure 15: Optimized design, potential, concentration  $c_1$ , and concentration  $c_2$  from left to right for case 4.2.

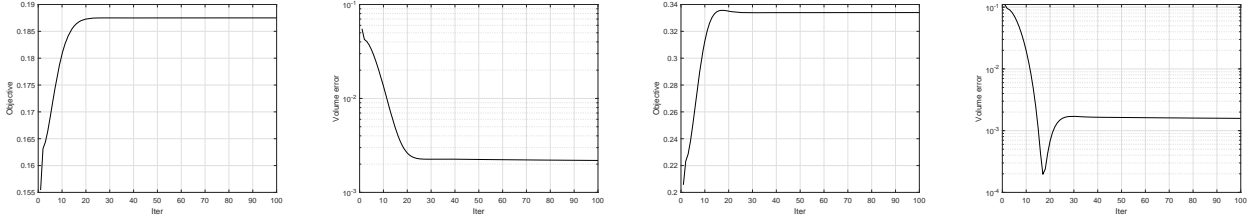


Figure 16: The convergence histories of objective and volume error (left 1, 2 for case 4.1 and right 1, 2 for case 4.2).

- [15] H.K. Gummel, A self-consistent iterative scheme for one-dimensional steady-state transistor calculations. IEEE Trans. Electr. Dev. ED-11, (1964) pp. 455–465.
- [16] J. Haslinger and R. Mäkinen, Introduction to Shape Optimization: Theory, Approximation, and Computation, SIAM, 2003.
- [17] J. Hadamard, M'emoire sur le probl'eme d'analyse relatif 'a l'equilibre des plaques 'elastiques encastr'ees, in: M'emoire des savants 'etrangers, 33 (1907).
- [18] F. Hecht, New development in FreeFem++. J. Numer. Math. 20 (2012) pp. 251–265.
- [19] J. A. Iglesias, K. Sturm and F. Wechsung, Two-dimensional shape optimization with nearly conformal transformations. SIAM J. Sci. Comput. 40 (2018) pp. 3807–3830.
- [20] N. Ishizuka, T. Yamada, K. Izui and S. Nishiwaki, Topology optimization for unifying deposit thickness in electroplating process. Struct. Multidiscip. Optim. 62 (2020) pp. 1767–1785.
- [21] J. Li and S. Zhu, Shape optimization of Navier–Stokes flows by a two-grid method. Comput. Methods Appl. Mech. Engrg. 400 (2022) 115531.
- [22] P.A. Markowich, The Stationary Semiconductor Device Equations, Springer, Wien, 1986.
- [23] S. Mitchell and M. Ortiz, Computational multiobjective topology optimization of silicon anode structures for lithium-ion batteries. J. Power Sources 326 (2016) pp. 242–251.
- [24] B. Mohammadi and O. Pironneau, Applied Shape Optimization for Fluids. Clarendon Press, Oxford, 2001.
- [25] S. Osher and F. Santosa, Level set methods for optimization problems involving geometry and constraints I. frequencies of a two-density inhomogeneous drum. J. Comput. Phys. 171 (2001) pp. 272–288.
- [26] J. Onishi, Y. Kametani, Y. Hasegawa, and N. Shikazono, Topology Optimization of Electrolyte-Electrode Interfaces of Solid Oxide Fuel Cells based on the Adjoint Method, J. Electrochem. 166 (2019) pp. F876–F888.
- [27] A. Prohl and M. Schmuck, Convergent discretizations for the Nernst-Planck-Poisson system, Numer. Math. 111 (2009) pp. 591–630.
- [28] T. Roy, M. Troya1, M. Worsley and V. Beck, Topology optimization for the design of porous electrodes, Struct. Multidiscip. Optim. 65 (2022) 171.
- [29] V. Schulz and M. Siebenborn, Computational comparison of surface metrics for PDE constrained shape optimization, Comput. Methods Appl. Math. 16 (2016) pp. 485–496.

- [30] J. Sokolowski and J.P. Zolésio, Introduction to Shape Optimization: Shape Sensitivity Analysis, Springer, Heidelberg, 1992.
- [31] K. Yaji, S. Yamasaki, S. Tsushima, T. Suzuki and K. Fujita, topology optimization for the design of flow fields in a redox flow battery, *Struct. Multidiscip. Optim.* 57 (2018) pp. 535-546.
- [32] G. Yoon and J. Park, Topological design of electrode shapes for dielectrophoresis based devices. *J. Electrostat.* 68 (2010) 475-486.
- [33] Q. Zhang, Q. Wang, L. Zhang and B. Lu, A class of finite element methods with averaging techniques for solving the three-dimensional drift-diffusion model in semiconductor device simulations, *J. Comput. Phys.* 458 (2022) 111086.
- [34] X. Zhang, Z. Kang and M. Li, Topology optimization of electrode coverage of piezoelectric thin-walled structures with CGVF control for minimizing, *Struct. Multidiscip. Optim.* 50 (2014) pp. 799-814.
- [35] S. Zhu, Effective shape optimization of Laplace eigenvalue problems using domain expressions of Eulerian derivatives. *J. Optim. Theory Appl.* 176 (2018) pp. 17-34.